Semi-Analytic Radiatively Inefficient Accretion Flows in General Gravity

by

Boris Georgiev

A thesis
presented to the University of Waterloo
in fulfillment of the
thesis requirement for the degree of
Master of Science
in
Physics

Waterloo, Ontario, Canada, 2017

I hereby declare that I am the sole author of this thesis. This is a true copy of the thesis, including any required final revisions, as accepted by my examiners.

I understand that my thesis may be made electronically available to the public.

Abstract

The Event Horizon Telescope is capable of observing black holes on event-horizon scales and we can use it to explore deviations from General Relativity. We replicate the results of a previous study using a Newtonian prescription of gravity to set a suitable limit to justify viscosity and radiation choices. We also create a framework to explore semi-analytic models of Radiatively Inefficient Accretion Flows with a covariant prescription of gravity. We study a Kerr-like metric not described by General Relativity, and find only small deviations from Kerr solutions. We also find that the dynamics of the flow are sensitive to small General Relativistic effects.

Acknowledgements

I thank my advisers, Avery Broderick and Luis Lehner, for their invaluable support and assistance to this project and thesis. I would also like to acknowledge the University of Waterloo and Perimeter Institute, which provided a wonderful working environment, and any sources of funding that made this work possible.

Table of Contents

List of Figures

Chapter 1

Introduction

Active galactic nuclei (AGN) are compact, highly-luminous regions found at centers of galaxies, and due to their measurable luminosity in all electromagnetic bands, they are excellent sources to explore gravity and accretion. The emission of AGN is expected to be the result of accretion [16] onto a supermassive black hole (SMBH) with many millions or billions of solar masses. Evidence for SMBHs comes primarily from measured star velocity dispersions, which show massive dark compact objects at centers of virtually all AGN [15]. Reverberation mapping, a technique that correlates time variability in an AGN, has estimated the black hole mass of about 40 AGN SMBHs. Proposed mechanisms for feeding this AGN accretion include stellar winds, galactic gas, and feedback. Some AGN have bright relativistic jets produced near the black hole, as has been observed by [10]. Possible mechanisms for generating these jets include high magnetic fields or frame dragging near the black hole event horizon. As such, AGN observations are heavily influenced by strong gravity effects near the black hole event horizon.

Our galaxy has a low-luminosity AGN, but due to its proximity and large angular size compared to other AGN, we have much information about its enviroment and astrophysical properties. Located at the center of our AGN is a radio-bright flat-spectrum source, which we call Sagittarius A* (Sgr A*). From observation of stellar trajectories, we know Sgr A* is the home of a $4.02 \pm 0.16 \pm 0.04 \times 10^6 M_\odot$ black hole [4]. Further observations of infrared flux and observed size place strong constraints on the existence of this SMBH [6]. From simulations of stellar wind dynamics, we believe Sgr A* is primarily fed by winds from stars in the central few parsecs of the galactic center [9]. The outer gas temperature that feeds the accretion has been determined through an optically-thin model and Chandra X-ray observations as 1.3 keV, with an electron number density of 100 cm^{-3} [2]. However, density measurements of the plasma a few Schwarzschild radii away from

Sgr A* from rotation measures are many orders of magnitude lower than we would expect from luminosity measurements [17]. Furthermore, we do not see as much radiation as we would expect for gas heated by gravitational accretion. We believe the energy is stored into ions, which do not efficiently give it to electrons. This leads us to believe that Sgr A* is characterized by a Radiatively Inefficient Accretion Flow (RIAF).

The Event Horizon Telescope (EHT) is a set of radio telescopes scattered across the globe to create an interferometer with Earth-sized baselines. The EHT looks at 230 and 345 GHz. At these frequencies, the apparent size of Sgr A* is 50 microarcseconds, which the EHT, capable of reaching resolutions of 10 microarcseconds, can resolve the event horizon of Sgr A*. The other candidate for EHT observations is Messier 87, which has a jet and is also expected to be surrounded by a RIAF. This emitting region is seemingly dominated by gravitational effects on lensing, dynamics, and structure. To extrapolate meaningful information about the gravity at play, we need to devise a model to map parameters to an image. This process takes two steps. First, we model the gas accretion using magnetohydrodamic and gravitational physical laws to get an accretion flow structure. Then, we ray trace photon paths and integrate the radiative transfer equations to turn that structure into a simulated image. We expect these images to look like Figure 1.1. Gravity plays a key role in the features of these images, and comparison to results of the EHT can provide meaningful information about gravity.

Accretion flows take the shape of spinning disks of ionized gas. The gas ionizes because the ions are hot and have low density. As it falls in, it eventually reaches the Innermost Stable Circular Orbit (ISCO), a key feature of black holes, and inside that radius, the gas must accrete. RIAFs assume the gas is optically thin, and therefore feels no radiative force. As the gas falls in, the ions get heated to upwards of 10^{11} K, but the electrons remain cooler. Only in the final few Schwarzschild radii do the electrons emit much radiation, making them excellent for viewing in the EHT observing bands. RIAFs are characterized by a large disk height, low luminosity, and a low accretion rate. The study in [22] has had success modeling the RIAF around Sgr A* with a mass accretion rate as a function of the radius away from the black hole to better account for an expected wind.

For the gas to fall into the black hole, it must transport its angular momentum to gas further out. From [3], we know the viscous effect is caused by the magnetorotational instability (MRI). The MRI is caused by shearing magnetic fields, which, in a rotating system, cause a destabilizing azimuthal force. Unlike gas collisional viscosity, this effect is strong enough to transport angular momentum outward on orbital timescales. In a RIAF, this effect heats the ions, which then transfer their energy to the electrons via Coulomb collisions, which radiate it away. In accretion flows, electrons are highly relativistic and have complicated radiation profiles that depend on the magnetic field. However, the mag-

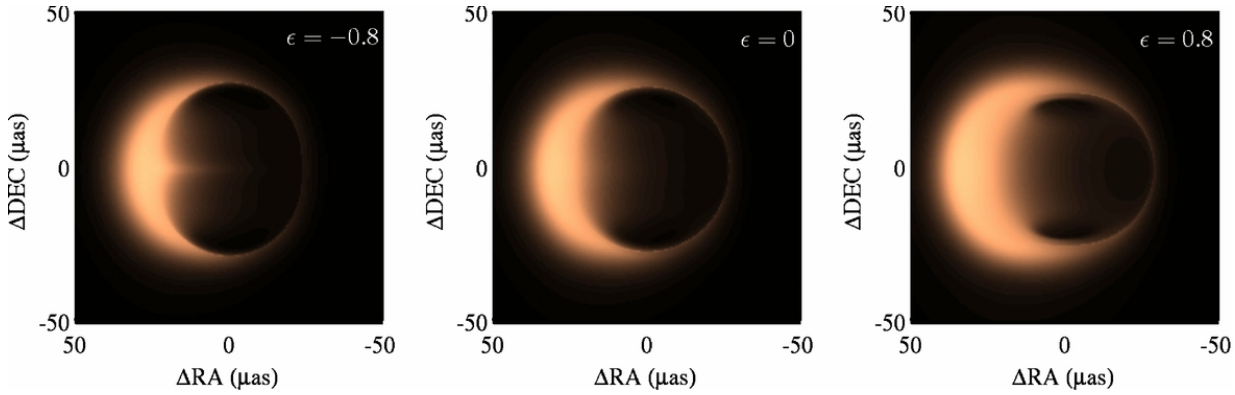

Figure 1.1: Model images of black hole for different quadrupole parameters
Simulated images showing the deviations to the image that would be seen by the EHT caused by adding a nonzero quadrupole moment, ϵ, to the black hole metric. The effects are strong enough to be detected by the EHT. Figure reprinted from [5].

netic fields are strong and the density low, so models usually restrict electrons to the most prominent sources of radiation: synchotron, Bremesstrahlung, and Compton cooling.

1.1 Previous Work

We wish to understand the deviations from General Relativity and relate them to observables. Figure 1.1 shows the effects of a quasi-Kerr metric on the shape of the apparent black hole shadow [5]. Subsequent tests [14] show that such metric perturbations could be detected with the EHT with sub-percent precision. However, these tests only applied the metric modifications while imaging. For the structure and dynamics of the accretion flow, [5] uses models similar to that in Section 3, with a quasi-Newtonian gravity prescription, without solving for the changes due to a modified metric. Therefore, in order to extrapolate meaningful conclusions about the effects of modified gravity on observation from the EHT, it becomes imperative to remove this source of systematic uncertainty.

In this work, we develop a code that can properly generate the structure and dynamics of an accretion flow for any metric.

1.2 A Note on Conventions

Throughout this work, we will use a metric with a signature of -1. All results and calculations will be done in cgs units, but the derivation in Chapter 4 will use $c = G = 1$ units. Note that unlike many texts, we use $r_g = 2GM/c^2$. For a description of concepts used from General Relativity, see, for example, [18]. Greek indices run over cylindrical Boyer-Lindquist coordinates. Matrices will be denoted as $\overline{\overline{\sigma}}$. In Chapters 3 and 4, the subscript, m, will denote the midplane value of quantities, such as the pressure or density, after height-integration, for example, ρ_m.

Chapter 2

Bondi Accretion

To properly understand how general gravity affects the structure and dynamics of accretion flows, it is useful to look at a model with minimal physics that still contains the characteristics of RIAFs. Bondi accretion is steady-state spherical accretion onto a gravitating object idealized as a point. There is a constant influx of gas at some far radius, which leaves the system through the central object. The physical mechanisms governing the gas flow are pressure, gravity, and radiation. For a further examination of Bondi accretion, see, for example, [11].

2.1 Eddington Limit

Consider a case of Bondi accretion with radiation pressure fully balancing gravity. The radial balance equation is

$$\frac{L\kappa}{c}\frac{1}{4\pi r^2} = \frac{GM}{r^2} \tag{2.1}$$

where L is the luminosity, κ is the opacity, and M is the mass of the central object. For ionized hydrogen, the opacity is given by Thomson scattering as $\kappa = \sigma_T/m_i$, where σ_T is the Thomson scattering cross section, and m_i is the ion mass. Equation (2.1) yields the Eddington luminosity

$$L_{\text{Edd}} = \frac{4\pi GMcm_i}{\sigma_T} \tag{2.2}$$

If the gas radiated any stronger, any gas fed in at the outer radius would immediately be pushed back out of the system. The corresponding maximum accretion rate is

$$\dot{M}_{\text{Edd}} = \frac{4\pi GMm_i}{\epsilon c \sigma_T} \tag{2.3}$$

where $\epsilon = 0.1$ is a typical value for the efficiency of transferring rest mass energy into radiation. Sgr A* accretes many orders of magnitude less than the Eddington mass accretion rate [2]. We can therefore assume that Sgr A* is indeed characterized by a RIAF, and that, for accretion flow models, radiation should not have a noticeable effect on the momentum conservation.

2.2 Critical Point

We now study the structure of the accretion flow. Since electromagnetic interactions yield an effective mean free path much smaller than the event horizon, the gas dynamics can be modeled with large-scale conservation equations rather than micro-physics. Spherical symmetry imposes all physical quantities are a function solely of the radius, and the steady-state condition imposes that at a given radius, the gas can only be described by one density, pressure, velocity, etc.

The gravitational potential is described by Newtonian theory as

$$\Phi = -\frac{GM}{r}. \tag{2.4}$$

Mass conservation is governed by the continuity equation in spherical coordinates

$$\dot{M} = -4\pi r^2 \rho v \tag{2.5}$$

where ρ and v are the density and outward radial velocity of the gas, respectively. $\dot{M}$ is the mass accretion rate supplied at some outer radius, and is constant. We will consider an ideal gas with a relativistic adiabatic coefficient, so the equation of state is

$$p = C\rho^{4/3} \tag{2.6}$$

for some proportionality constant, C. All gas dynamics is captured by the Euler equation

$$\frac{\partial \vec{v}}{\partial t} + \vec{v} \cdot \vec{\nabla}\vec{v} = -\frac{1}{\rho}\vec{\nabla}p - \vec{\nabla}\Phi. \tag{2.7}$$

Since the flow is steady state, all the time derivatives are zero. We can impose spherical symmetry and take only the radial component

$$v\frac{dv}{dr} = -\frac{1}{\rho}\frac{dp}{dr} - \frac{GM}{r^2} \tag{2.8}$$

From 2.5 and 2.6, we can write

$$\frac{dp}{dr} = \frac{4}{3}C\rho^{1/3}\frac{\dot{M}}{4\pi}\left(\frac{2}{r^3 v} - \frac{1}{r^2 v^2}\frac{dv}{dr}\right) = -c_s^2\rho\left(\frac{2}{r} - \frac{1}{v}\frac{dv}{dr}\right) \tag{2.9}$$

where the gas sound speed,

$$c_s = \sqrt{\frac{4}{3}\frac{p}{\rho}} \tag{2.10}$$

is chosen as $c_s = dp/d\rho$ to make the critical point at $v = c_s$. Combining equation (2.9) with equation (2.8), with aid from a computer algebra program, the conservation of momentum equation can be written as

$$\left(1 - \frac{c_s^2}{v^2}\right) v\frac{\partial v}{\partial r} = -\frac{GM}{r^2}\left(1 - \frac{2c_s^2 r}{GM}\right). \tag{2.11}$$

Note that at $v = c_s$, and $r = r_s = GM/2c_s^2$, the sonic radius, the solution becomes ill-defined. This corresponds to a critical saddle point dividing the set of solutions. The solution we are interested in is one passing through that critical point.

This model is now a boundary value problem that we can numerically integrate. Upon writing equation (2.11) in terms of the normalized quantities v/c_s and r/r_s, all dependence on the parameters, $\dot{M}$, M, and C, cancels. A phase plot of the velocity of the gas as a function of radius is shown in Figure 2.1. Each curve plotted represents a solution to our differential equation for some initial gas position and velocity. There are six types of solutions, but not all are physical. We have assumed that at any radius, the gas can have one velocity, so solutions of type III or IV are only valid until they turn around in radius. In a physical case, turbulence from gas flowing in different directions would shift the initial conditions down to a curve passing through the critical point. Type I solutions occur when the gas is entering our system supersonically, and cannot stabilize into a flow. Any perturbation would remain, as no information can travel through the gas, thus violating the steady-state condition. Type II solutions correspond to gas pressure overcoming gravity. These solutions can be stable, but develop into critical flows [12].

There are two stable solutions: indicated in Figure 2.1 by curves (a) and (b), which are an accretion flow and wind solution, respectively. We assume our flow begins close to

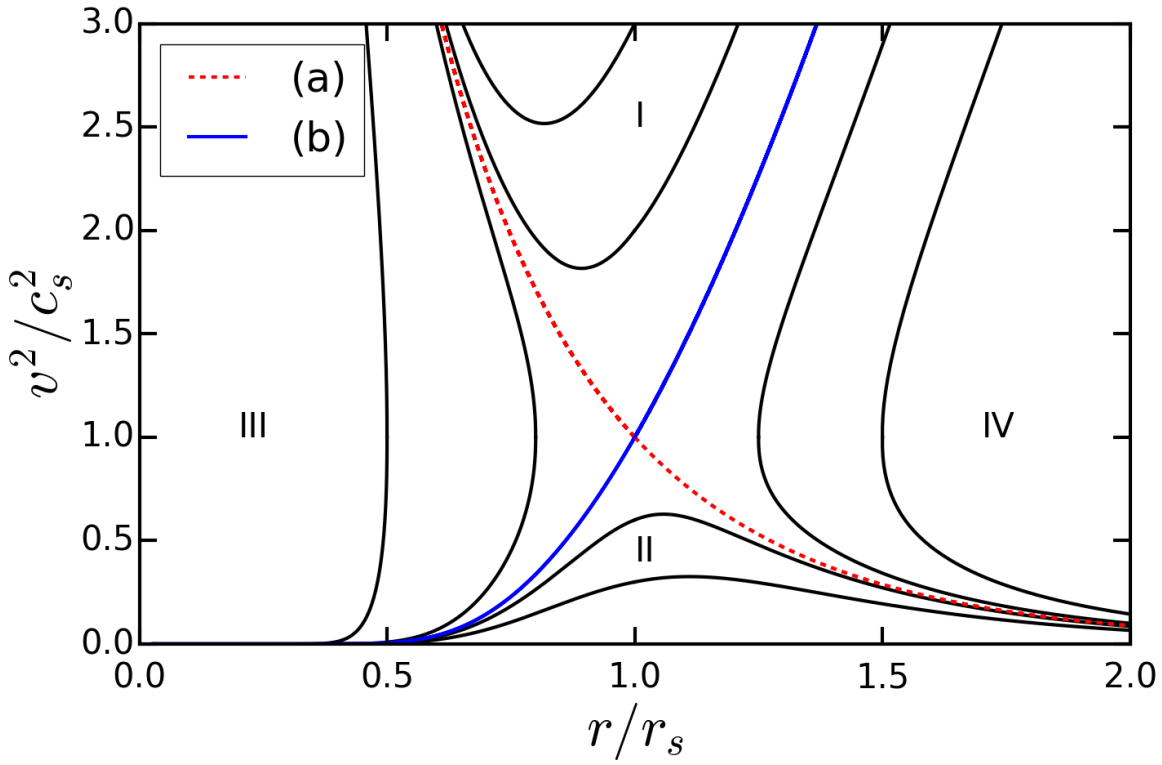

Figure 2.1: Bondi accretion phase plot

Plot of velocity versus radius. There are six different types of solutions. With the steady-state condition, only two solutions are valid. Curve (a) corresponds to an accretion flow, and curve (b) is a wind solution.

rest far away, and enters the black hole supersonically, represented in Figure 2.1 by a low velocity at large radius. Note that, in an accretion flow with shocks allowed, parts of a stable gas solution could jump to a black curve, and exhibit non-flow behavior. However, the steady state condition allows us to ignore all flow solutions except (a). We expect more intricate models to still exhibit this critical point behavior, and contain only one accretion flow solution.

Chapter 3

Newtonian Model

The Bondi accretion flow model in Section 2.2 is highly idealized, and we will attempt to add faithfullness by introducing electromagnetic fields, viscosity, rotation and gravity more closely resembling a black hole.

We expect any electrostatic imbalance to be corrected in a short timescale, so we will neglect such effects. Accretion flows are, however, expected to be heavily impacted by magnetic fields. As the gas rotates inward, magnetic fields will become twisted and highly sheared. The steady-state condition allows us to only consider local effects of the magnetic field. It will be responsible for radiation and for viscous heating and angular momentum transport through the MRI.

We are dealing with a RIAF, so we must model the gas ions and electrons separately, to allow an energetic gas to radiate inefficiently. We will add mechanisms for the gas to heat, transfer energy, and radiate. Heating will be determined by our choice for magnetic shear, and energy transport between ions and electrons will be dominated by Coulomb collisions.

The following analysis closely follows Yuan et al. [21].

3.1 Derivation of Governing Equations

Motivated by angular momentum conservation coupled with the steady-state condition, the spherical flow will be replaced with an axisymmetric flow, and the variable r will now refer to the cylindrical radius. The flow will resemble a disk, where at a given radius, the gas will have some vertical height. Although this will be a geometrically thick disk, we

will impose $z^2 \ll r^2$ and $v_z \ll v_r$ for simplicity. More commentary on the consequences of this choice is available in Section 5.3. While we will still use a Newtonian-like prescription of gravity, we wish to make use of a modified potential that captures some of the physical effects associated with black holes in general relativity. A key effect is the existence of an Innermost Stable Circular Orbit, inside of which the gas will accrete even without angular momentum transport. To that end, we will introduce the Paczyński-Wiita potential

$$\Phi = -\frac{GM}{r - r_g} \tag{3.1}$$

where $r_g = 2GM/c^2$ is the black hole Schwarzschild radius. This potential contains an event horizon, and an ISCO.

We consider a randomly oriented magnetic field everywhere, such that the magnetic pressure is proportional to the gas pressure with a constant ratio. That is,

$$p = p_{\rm tot} = p_{\rm gas} + p_{\rm mag} = p_{\rm gas} + \frac{1-\beta}{\beta} p_{\rm gas} = \frac{p_{\rm gas}}{\beta}. \tag{3.2}$$

Assuming an optically-thin two-temperature ideal gas, we can write the gas pressure as

$$p_{\rm gas} = \frac{\rho}{\mu_i} \frac{k_B}{m_\mu} T_i + \frac{\rho}{\mu_e} \frac{k_B}{m_\mu} T_e \tag{3.3}$$

in which ρ is the density of the gas, T_i and T_e are the ion and electron temperatures, respectively, and k_B is the Boltzmann constant. For ionized hydrogen, we can set the effective molecular mass to the ion mass, $m_\mu = m_i$. The mean molecular weights are

$$\mu_i = 1.23 \qquad\qquad \mu_e = 1.13. \tag{3.4}$$

For simplicity, we assume the gas density and pressure can be characterized by a midplane value and a scale height. Further equations can be height-integrated to create one-dimensional equations of midplane values. More specifically, we will apply a height-integration operator,

$$\mathcal{O}_{HI}(f) = \frac{1}{2H} \int_{-H}^{H} f dz \tag{3.5}$$

to all equations, sometimes implicitly.

We can solve for the scale height from the vertical balance equation

$$\frac{dp}{dz} = -\rho \Omega_K^2 z \tag{3.6}$$

where $\Omega_K = \sqrt{GM/(r-r_g)^2 r}$ is the Keplerian angular velocity. Assuming some vertical distribution

$$H = \frac{c_s}{\Omega_K} \tag{3.7}$$

where $c_s = \sqrt{p/\rho}$ is the gas soundspeed, defined differently than before to agree with the literature.

3.1.1 Viscosity

The disk will be allowed to rotate, and magnetic viscosity between successive cylindrical shells of gas will heat the ions. From the MRI, we know that the viscosity should go as $\langle B^r B^\phi \rangle$. However, the magnetic field is heavily twisted and sheared such that $B^r \propto B^\phi$. From

$$\langle B^r B^\phi \rangle \propto \langle B^r B^r \rangle \propto p_{\rm mag} \tag{3.8}$$

we are motivated to try a choice of viscosity proportional to pressure known as the α-viscosity prescription. This approximation of the MRI has had success in previous models of accretions flows [20]. This argument allows us to approximate the shear tensor component

$$\sigma_{r\phi} = \rho\nu r^2 \frac{\partial\Omega}{\partial r} \tag{3.9}$$

as

$$\sigma_{r\phi} = -\alpha r p \tag{3.10}$$

where α is constant. Note that this definition of $\sigma_{r\phi}$ differs from the one employed in [11] due to different definitions of $\hat{\phi}$. We will ignore all other shear tensor components. Accretion theory commonly uses the α-disk prescription of

$$\nu = \alpha c_s H = \frac{\alpha}{\Omega_K}\frac{p}{\rho} \tag{3.11}$$

as in [11] and [20], which we will not be studying to agree with [21], although the two different viscosity prescriptions can be subtly similar for thick disks [1]. Our choice for the stress tensor imposes $\sigma_{r\phi}$ vanish at the event horizon. Thus, the inability of the event horizon to torque the gas in a steady-steady flow is explicit in our viscosity prescription.

3.1.2 Conservation Equations

The equations that govern the gas dynamics arise from conservation of mass, momentum, and energy. Similar to equation (2.5), the mass conservation equation is

$$\dot{M} = -4\pi r H \rho v. \tag{3.12}$$

The momentum conservation equations use a modified Euler equation

$$\rho \frac{\partial \vec{v}}{\partial t} + \rho(\vec{v} \cdot \nabla)\vec{v} = -\nabla p - \rho \nabla \Phi + \nabla \cdot \overline{\overline{\sigma}} \tag{3.13}$$

in which the stress tensor, $\overline{\overline{\sigma}}$, has only one nonzero component, $\sigma_{r\phi}$ as defined in Section 3.1.1. Using axisymmetry, the steady-state condition, and our vertical prescription, we can write the radial momentum equation as

$$\rho v \frac{dv}{dr} - \rho r \Omega^2 = -\frac{dp}{dr} - \rho \frac{d\Phi}{dr} \tag{3.14}$$

in which v now refers to the outward radial velocity. We wish to height-integrate this equation, but we must consider the change in gravity away from the midplane, as we know the vertical dependence of the gravitational potential, and cannot approximate it with a scale height. We can write the gravitational potential as

$$\Phi = \Phi(z = 0) + \frac{\Omega_K^2 z^2}{2}. \tag{3.15}$$

Upon height-averaging of equation (3.14), we encounter

$$\int \left(\rho \frac{d}{dr} \left(\frac{\Omega_K^2 z^2}{2} \right) \right) dz = \frac{d\Omega_K}{dr} \int \left(\rho \Omega_K z^2 \right) dz = \\ - \frac{1}{\Omega_K} \frac{d\Omega_K}{dr} \int \frac{dp}{dz} z dz = \frac{1}{\Omega_K} \frac{d\Omega_K}{dr} \int p dz \tag{3.16}$$

where we have used the vertical balance equation, equation (3.6). Therefore, we can write equation (3.14) as

$$\rho_m v \frac{dv}{dr} - \rho_m r \Omega^2 = -\frac{1}{H} \frac{d(p_m H)}{dr} - \rho_m r \Omega_K^2 + \frac{1}{\Omega_K} \frac{d\Omega_K}{dr} p_m \tag{3.17}$$

in which the subscript m denotes the midplane value. Combining this with equation (3.7), we get

$$v \frac{dv}{dr} + c_s \frac{dc_s}{dr} = -\Omega_K^2 r + \Omega^2 r - \frac{1}{\rho_m} \frac{dp_m}{dr}. \tag{3.18}$$

From equation (3.13) in the azimuthal direction, we have

$$\rho v \frac{d\left(r\Omega\right)}{dr} + \rho \Omega v = \frac{1}{r^2}\frac{d}{dr}(r\sigma_{r\phi}) \tag{3.19}$$

$$\rho v r \frac{d\left(r^2\Omega\right)}{dr} = -\frac{d}{dr}(\alpha r^2 p) \tag{3.20}$$

where we have used the viscosity prescription in equation (3.10). We can, again, height-integrate

$$\rho_m H v r \frac{d\left(r^2\Omega\right)}{dr} = -\frac{d}{dr}(\alpha r^2 p_m H) \tag{3.21}$$

The term $\rho_m H v r$ is proportional to $\dot{M}$, which we assume is constant, so this equation can be integrated analytically.

$$v\left(\Omega r^2 - j\right) = -\alpha r \frac{p_m}{\rho_m}. \tag{3.22}$$

j is an angular momentum eigenvalue, but because our viscosity prescription imposes the torque vanish at the event horizon, it is equal to the angular momentum at the event horizon. By integrating analytically, we have replaced a boundary condition on the angular momentum with a condition of the flow passing through the critical point.

From thermodynamic laws, we can write the ion and electron energy equations as

$$\rho v \left(\frac{d\varepsilon_i}{dr} + p_i \frac{d}{dr}\left(\frac{1}{\rho}\right)\right) = -\alpha p r \frac{d\Omega}{dr} - q_{ie} \tag{3.23}$$

$$\rho v \left(\frac{d\varepsilon_e}{dr} + p_e \frac{d}{dr}\left(\frac{1}{\rho}\right)\right) = q_{ie} - q^- \tag{3.24}$$

where terms on the left are the adiabatic evolution of the gas, and the right hand side contains heating, cooling, and energy exchanges. To height-integrate, we will make the transformation $\rho \to \rho_m$, and $p \to p_m$. By doing this instead of properly integrating, we are essentially claiming we can use

$$p_m \frac{\partial}{\partial r}\left(\frac{1}{\rho_m}\right) \tag{3.25}$$

instead of

$$p_m H \frac{\partial}{\partial r}\left(\frac{1}{\rho_m H}\right) = p_m \frac{\partial}{\partial r}\left(\frac{1}{\rho_m}\right) - \frac{p_m}{\rho_m}\frac{1}{H}\frac{\partial H}{\partial r} \tag{3.26}$$

and removing a term that will make a significant impact. However, we will neglect it to remain a replica of [21]. The energies of the ions and electrons are

$$\varepsilon_i = \frac{3}{2}\frac{k_B T_i}{\mu_i m_\mu} \tag{3.27}$$

$$\varepsilon_e = a_e \frac{k_B T_e}{\mu_e m_\mu}. \tag{3.28}$$

Because the electrons will become relativistic, we introduce the relativistic adiabatic coefficient,

$$a_e = \frac{1}{\theta_e}\left[\frac{3K_3\left(\frac{1}{\theta_e}\right) + K_1\left(\frac{1}{\theta_e}\right)}{4K_2\left(\frac{1}{\theta_e}\right)} - 1\right] \tag{3.29}$$

where K_3, K_1, K_2 are modified Bessel functions of the second kind of order 3, 1, and 2, respectively, and $\theta_e = k_B T_e / m_e c^2$[8].

The energy flux from the ions to the electrons via Coulomb collisions is given by [21]

$$q_{ie} = \frac{3}{2}\frac{m_e}{m_i} n_e n_i \sigma_T c \ln\Lambda \left(k_B T_i - k_B T_e\right) \frac{\sqrt{\frac{2}{\pi}} + \sqrt{\theta_i + \theta_e}}{\left(\theta_i + \theta_e\right)^{3/2}} \tag{3.30}$$

where $\theta_i = k_B T_i / m_i c^2$, n is the number density, and $\ln\Lambda = 20$ is the Coulomb logarithm. The gas has low density, strong magnetic fields, and the electrons are highly relativistic. Therefore, we assume our radiative cooling occurs only by synchotron radiation. To derive the energy lost, begin with the power emitted from one electron [19]

$$P = \frac{4}{3}\sigma_T c \frac{B^2}{8\pi}\gamma^2 \tag{3.31}$$

where γ is the relativistic Lorentz factor. We choose the distribution of electrons to be thermal

$$f(\gamma) = \frac{n_e}{2\theta_e^2} e^{-\gamma/\theta_e}\gamma^2 \tag{3.32}$$

where the distribution has been normalized to $n_e = \rho/m_i$, as the number densities of both electrons and ions are assumed to be the same with the steady-state condition. We now have the energy lost due to radiation as

$$q^- = \int P f(\gamma) d\gamma = \int_0^\infty \left(\frac{4}{3}\sigma_T c \frac{B^2}{8\pi}\gamma^2 \frac{n_e}{2\theta_e^2} e^{-\gamma/\theta_e}\gamma^2\right) d\gamma = \frac{2\sigma_T c \rho B^2 \theta_e^2}{\pi m_e} \tag{3.33}$$

Since the magnetic pressure is related to the total pressure by a factor of $1-\beta$, we have

$$q^- = \frac{16\sigma_T c\theta_e^2(1-\beta)p\rho}{m_e} \tag{3.34}$$

Analytically, this term has a small effect on electron temperature, which in turn has a small affect on other quantities of the flow. We argue that the different choice for the cooling prescription should not have an effect on the structure deviations for a perturbed metric. Similarly, q_{ie} is subleading in equation (3.23) and any effects on the ion temperature will be insignificant. This idea is reinforced by running tests with cooling removed, so that electrons do not lose energy, and finding only small deviations only to T_e. Therefore, while our model does yield a convincing velocity and ion temperature profile, a study of radiative flux or a spectrum would require more precise energy transfer expressions.

3.2 Accretion Flow Solutions

We have improved upon the model in Section 2.2, but we still only have a set of differential equations to solve. Three of the boundary conditions - the mach number, and ion and electron temperature - were set at some outer radius defined at 1000 r_g. This radius was chosen to be sufficiently far away from gravitational effects, to better model the ambient gas in the galactic center. The condition for j was found by integrating inward and using bisection to approximate the value necessary for the solution to go through the critical point. Figure 3.2 shows data from [21] for structure solutions with certain boundary conditions and parameters. Figure 3.1 is our figure that demonstrates our code can reliably reproduce the solutions of [21]. There is a discrepancy with the electron temperature at low radii. However running the simulation with $q^- = 0$ returns a nearly identical solution with the electron temperature slightly above that of [21]. This reaffirms our assumption that the cooling prescription has little impact on the flow, and we conclude that we can reproduce the solutions of [21] up to different choices for cooling.

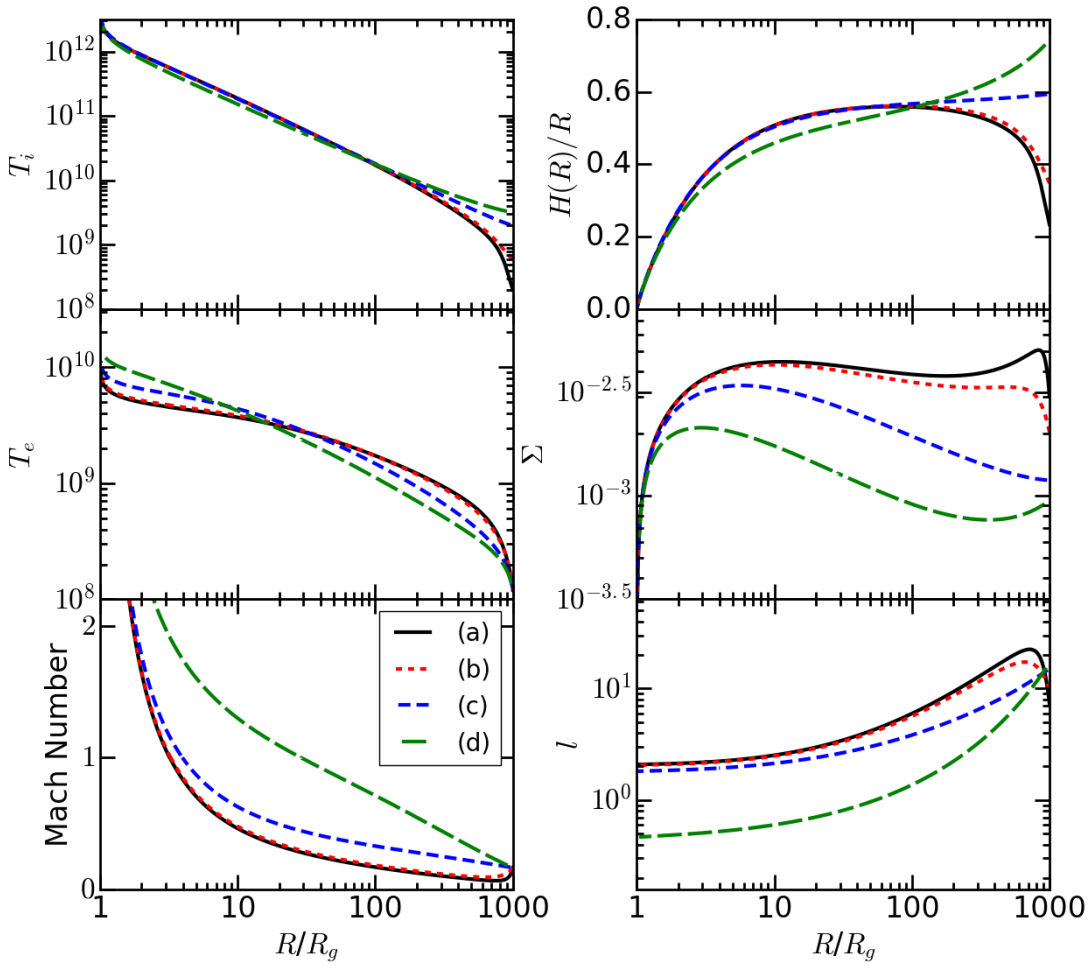

Figure 3.1: Effects of varying outer boundary conditions on accretion flow solutions. This plot is a replication of the accretion flow structure from Yuan et al. The initial conditions are exactly as in Figure 3.2. The Mach number is defined as $-v/c_s/\sqrt{(3+\alpha^2)/2}$ to make the critical point at a Mach number of 1. The surface density, $\Sigma = 2H\rho_m$, and the angular momentum, $l = \Omega r^2 c/GM$. With the exception of the electron energy, these quantities agree with those of [21]. From the electron temperature, we can see that the cooling differences are only evident in T_e.

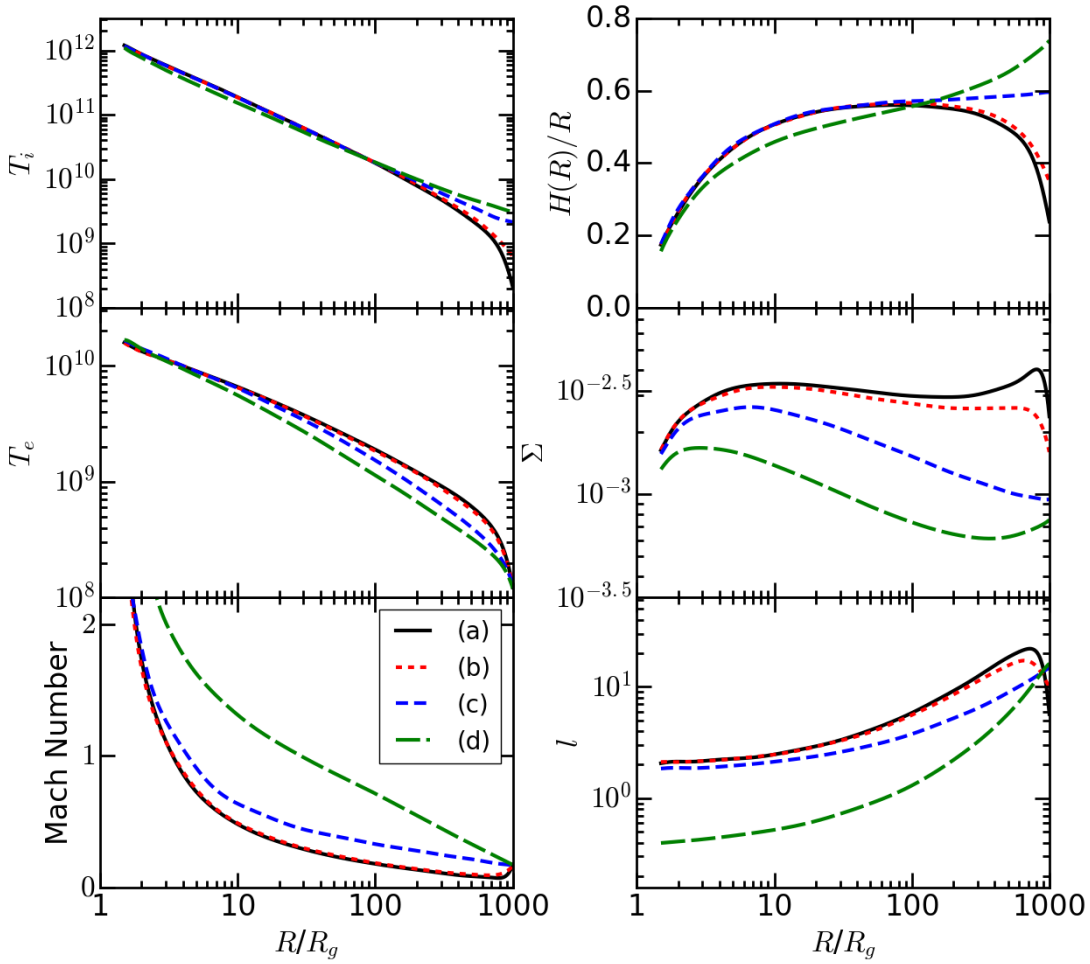

Figure 3.2: Replicated plot of accretion flow solutions
Data was taken manually from [21] and fit with a polynomial curve. All initial conditions and parameters used are the same as in Figure 1 of [21]. All solutions have $M = 10^9 M_\odot$, $\dot{M} = 10^{-4}\dot{M}_{\rm Edd}$, $\alpha = 0.1$, and $\beta = 0.9$. The boundary conditions are set at $r = 10^3 r_g$ as $v_{\rm out}/c_{s,\rm out} = 0.2$ and $T_{e,\rm out} = 1.2 \times 10^8 K$. In increasing alphabetic order, the outer ion temperature is set at $2 \times 10^8 K$, $6 \times 10^8 K$, $2 \times 10^9 K$, and $3.2 \times 10^9 K$.

Chapter 4

Covariant Model

Recall that the ultimate goal of this project is to test the influence of modified gravity on the semi-analytic accretion flow solutions. We assume gravity modifications can be described by extensions to General Relativity and captured by perturbations to the metric tensor. In particular, we implement a covariant prescription of gravity into the model, so that we can model the accretion flow with a general metric tensor. We can also apply this model's fully general relativistic description to more appropriately study black hole accretion flows.

4.1 Derivation

We will introduce the analog of the gas density as the rest mass density plus some energy density counterpart, that is

$$\rho = \rho_0 + \varepsilon_i + \varepsilon_e \tag{4.1}$$

where

$$\varepsilon_i = a_i \frac{\rho_0 k_B T_i}{\mu_i m_\mu} \tag{4.2}$$

$$\varepsilon_e = a_e \frac{\rho_0 k_B T_e}{\mu_e m_\mu}. \tag{4.3}$$

Unlike the model in Chapter 3, both the ions and electrons will be allowed to be relativistic. a_e takes the form of equation (3.29), and a similar definition is used for a_i. The magnetic

contribution to the pressure will be defined as in equation (3.2), and the gas pressure will be proportional to the rest mass density

$$p_{\text{gas}} = \frac{\rho_0}{\mu_i}\frac{k_B}{m_\mu}T_i + \frac{\rho_0}{\mu_e}\frac{k_B}{m_\mu}T_e. \tag{4.4}$$

We perform the following derivation in cylindrical Boyer-Lindquist coordinates. The local gas 4-velocity, u^α must obey $u^\alpha u_\alpha = -1$, and by vertical symmetry, $u^z = 0$ in the midplane. The temporal and azimuthal symmetries give rise to Killing vectors in t and z.

4.1.1 The Energy Momentum Tensor

Each of the conservation equations in the previous model have covariant counterparts. The continuity equation is

$$\nabla_\alpha (\rho_0 u^\alpha) = 0 \tag{4.5}$$

and for energy-momentum conservation, we have

$$\nabla_\alpha T^{\alpha\beta} = 0 \tag{4.6}$$

where $T^{\alpha\beta}$ is the energy-momentum tensor. For an ideal gas, the energy-momentum tensor is

$$T^{\alpha\beta}_{\text{ideal}} = (\rho + p)u^\alpha u^\beta + p g^{\alpha\beta}. \tag{4.7}$$

However, we want to encompass viscosity and radiation, so we will add linearly independent first order terms in ∇u:

$$\{g^{\alpha\beta}\nabla_\mu u^\mu, u^\alpha u_\mu \nabla^\mu u^\beta, u^\alpha u^\beta \nabla_\mu u^\mu, \nabla^\alpha u^\beta, u^\alpha u_\mu \nabla^\beta u^\mu\} \tag{4.8}$$

where α and β are symmetrized. Note the last term is zero, since $u_\mu \nabla^\beta u^\mu = 0$. We can choose any linear combination of these and of the terms in the ideal energy-momentum tensor so long as we are adding four new distinct terms to the ideal energy-momentum tensor. We rewrite them as

$$\{h^{\alpha\beta}\nabla_\mu u^\mu, u^\alpha q^\beta, u^\alpha u^\beta \nabla_\mu u^\mu, \sigma^{\alpha\beta}\} \tag{4.9}$$

where

$$h^{\alpha\beta} = g^{\alpha\beta} + u^\alpha u^\beta \tag{4.10}$$

is the projection tensor orthogonal to u^α. The first term is orthogonal to u^α, and goes as the divergence of the velocity. It is the bulk viscosity, and we will assume our gas has none. In the second term, we have defined the radiation flux as

$$q^\beta \propto u^\mu \nabla_\mu u^\beta \tag{4.11}$$

so that $q^\beta u_\beta = 0$. The third term is not orthogonal to u^α. The definition of ρ is

$$\rho = T^{\alpha\beta} u_\alpha u_\beta. \tag{4.12}$$

The third term changes ρ to include $\nabla_\mu u^\mu$. We have already used the idea of augmenting the density for a non-ideal gas in equation (4.1), using physical reasoning to determine its exact form. The last term is the shear viscosity. The definition is

$$\sigma_{\alpha\beta} = \frac{1}{2}\left(h^\mu_\alpha \nabla_\mu u_\beta + h^\mu_\beta \nabla_\mu u_\alpha\right) - \frac{1}{3} h_{\alpha\beta} \nabla_\mu u^\mu. \tag{4.13}$$

It is the traceless and symmetric part of $\nabla_\alpha u_\beta$ projected orthogonal to u^μ in both indices. This shear tensor may have causality issues, but we can remove them by constructing $t_{\alpha\beta}$ using the α viscosity prescription in Section 4.1.2. Combining these ideas, we can construct the energy momentum tensor

$$T^{\alpha\beta} = (\rho + p) u^\alpha u^\beta + p g^{\alpha\beta} + t^{\alpha\beta} + q^\alpha u^\beta + u^\alpha q^\beta \tag{4.14}$$

with

$$t_{\alpha\beta} = -2\rho_0 \nu \sigma_{\alpha\beta} \tag{4.15}$$

where ν is a viscosity coefficient.

For the physical cases considered, the gas accretes far lower than the Eddington rate, so radiation pressure should not contribute to the gas momentum. Therefore, we will ignore any contribution of terms involving q^α in the momentum balance equations.

4.1.2 Viscosity Prescription

We have to construct the tensor, $t_{\alpha\beta}$ using physical arguments. For numerical simplicity, we will only consider leading components of $\sigma_{\alpha\beta}$. The majority of the flow can be approximated by using the flat space metric, and is relativistic, but slow. We have $u^t \to 1 + v^2$, $u^r \to v$, and $r u^\phi \to u_\phi / r \to v$. The leading component is

$$\sigma_{r\phi} = \frac{1}{2}\left(h^\mu_r \nabla_\mu u_\phi + h^\mu_\phi \nabla_\mu u_r\right) = \frac{1}{2}\left(\partial_r u_\phi - \Gamma^\phi_{r\phi} u_\phi - \Gamma^\phi_{r\phi} u_\phi\right) \tag{4.16}$$

$$= \frac{1}{2}\left(\partial_r u_\phi - \frac{2u_\phi}{r}\right) = \frac{1}{2} r^2 \partial_r \left(\frac{u_\phi}{r^2}\right) = \frac{1}{2} r^2 \partial_r \Omega \tag{4.17}$$

This is precisely the shear term in the Newtonian limit. All other shear terms have leading terms of u^r, $\partial_r u^r$, or $\partial_r u^t$, and are subleading to $\sigma_{r\phi}$. For this flow, the angular velocity will dominate, so we will set all other shear components to zero. As well, $t_{\alpha\beta}$ must converge to its Newtonian counterpart and we will satisfy this condition by setting

$$t^r_\phi = \alpha r p. \tag{4.18}$$

4.1.3 Mass Conservation

The gas will be fed at some outer radius uniformly spread out over a cylinder. The continuity equation, equation (4.5), can be rewritten as

$$\frac{1}{\sqrt{-g}}\partial_\alpha\left(\sqrt{-g}\rho_0 u^\alpha\right) = 0. \tag{4.19}$$

We can integrate this over our outer cylinder, so we define the normal vector to this boundary as orthogonal to the t and ϕ Killing vectors and to a z unit vector:

$$\xi^\alpha n_\alpha = 0 \tag{4.20}$$

and since $\xi^\alpha = (1,0,0,0)$ and $\xi^\alpha = (0,0,1,0)$, $n_\alpha = (0,-1,0,0)$. Applying the divergence theorem to equation (4.19),

$$\dot{M} = \int \partial_t\left(\sqrt{-g}\rho_0 u^t\right) dV = \int \rho_0 u^\alpha n_\alpha \sqrt{-g} d\phi dz \tag{4.21}$$

$$= -4\pi\rho_{0,m} H u^r \sqrt{-g} \tag{4.22}$$

where the subscript, m, refers to the midplane value, and $\dot{M}$ is the mass accretion rate. Note that there is no equation that constrains $\dot{M}$ to be constant. Due to an expected wind, we can approximate the mass accretion rate with a power law [22]

$$\dot{M} = \dot{M}_{\text{out}}\left(\frac{r}{r_{\text{out}}}\right)^s. \tag{4.23}$$

We have chosen a power law for simplicity, but more comprehensive models can easily be implemented.

Next, we will split equation (4.6) into a components projected along u^α, in the direction of the ϕ Killing field, and projected along the r and z directions. The covariant conservation

equations we must solve are

$$h^r_\beta \nabla_\alpha T^{\alpha\beta} = 0 \tag{4.24}$$
$$h^z_\beta \nabla_\alpha T^{\alpha\beta} = 0 \tag{4.25}$$
$$\xi_\beta \nabla_\alpha T^{\alpha\beta} = 0 \rightarrow \nabla_\alpha \left(T^{\alpha\beta}\xi_\beta\right) = 0 \tag{4.26}$$
$$u_\beta \nabla_\alpha T^{\alpha\beta} = 0 \tag{4.27}$$

where ξ_β is the ϕ Killing vector.

4.1.4 Vertical Momentum

Similar to the Newtonian model, we want to have a one-dimensional problem in r. In the vertical direction, we assume $z \ll r$. That is, we will implicitly expand every term in z to second order until after height-integration. The Christoffel symbols will be notated as

$$\Gamma^\alpha_{\beta\gamma} = \Gamma^{\alpha\ (0)}_{\beta\gamma} + \Gamma^{\alpha\ (1)}_{\beta\gamma} z + \Gamma^{\alpha\ (2)}_{\beta\gamma} z^2 ... \tag{4.28}$$

To properly calculate these symbols, we must keep second-order terms of z in the metric in cylindrical coordinates. This leads to nonzero g^{zr} and z derivatives of the metric.

We write the vertical balance equation

$$\delta^z_\mu h^\mu_\beta \nabla_\alpha \left[(\rho + p)u^\alpha u^\beta + p g^{\alpha\beta} + t^{\alpha\beta} + q^\alpha u^\beta + u^\alpha q^\beta\right] = 0 \tag{4.29}$$
$$\delta^z_\mu \left[-(\rho + p)u^\alpha u^\beta \nabla_\alpha h^\mu_\beta + h^{\mu\alpha}\nabla_\alpha p\right] + \delta^z_\beta \nabla_\alpha \left(t^{\alpha\beta} + q^\alpha u^\beta + u^\alpha q^\beta\right) = 0 \tag{4.30}$$
$$\delta^z_\mu \left[(\rho + p)u^\alpha \nabla_\alpha u^\mu + h^{\mu\alpha}\partial_\alpha p\right] = 0 \tag{4.31}$$
$$(\rho + p)u^\alpha \Gamma^z_{\alpha\mu} u^\mu + g^{zz}\partial_z p + g^{zr}\partial_r p = 0 \tag{4.32}$$

where we have repeatedly used $h^{\alpha\beta}u_\beta = 0$ and $u^z = 0$. We can disregard the $g^{zr}\partial_r$ term, because it is of order $(z/r)^2 g^{zz}\partial_z$. As such, we can write

$$\partial_z p = -(\rho + p)\frac{\Gamma^{z\ (1)}_{\alpha\mu} u^\alpha u^\mu}{g^{zz}} z. \tag{4.33}$$

This looks similar to the Newtonian equation, equation (3.6), so we will assume the same vertical prescription. The pressure and density will have a midplane value, and a scale height defined by

$$H = \sqrt{\frac{p g^{zz}}{(\rho + p)\Gamma^{z\ (1)}_{\alpha\mu} u^\alpha u^\mu}}. \tag{4.34}$$

Height-integrating will be similarly performed, and equations that do not change under height-integration will not be explicitly shown.

4.1.5 Radial Momentum

The momentum conservation in the radial direction is:

$$\delta^r_\mu h^\mu_\beta \nabla_\alpha \left[(\rho+p)u^\alpha u^\beta + p g^{\alpha\beta} + t^{\alpha\beta}\right] = 0 \tag{4.35}$$

$$\delta^r_\mu \left[-(\rho+p)u^\alpha u^\beta \nabla_\alpha h^\mu_\beta + h^{\mu\beta}\nabla_\beta p + h^\mu_\beta \nabla_\alpha t^{\alpha\beta}\right] = 0 \tag{4.36}$$

$$\begin{aligned}\delta^r_\mu (\rho+p)u^\alpha \nabla_\alpha u^\mu + h^{r\beta}\partial_\beta p + \\ \delta^r_\mu \left[-u^\mu t^{\alpha\beta}\nabla_\alpha u_\beta + \delta^\mu_\beta \frac{1}{\sqrt{-g}}\partial_\alpha\left(\sqrt{-g}t^{\alpha\beta}\right) + \Gamma^\mu_{\alpha\nu} t^{\alpha\nu}\right] = 0\end{aligned} \tag{4.37}$$

$$(\rho+p)\left(u^r\partial_r u^r + \Gamma^r_{\alpha\mu}u^\alpha u^\mu\right) + h^{rr}\partial_r p - u^r t^{\alpha\beta}\sigma_{\alpha\beta} = 0 \tag{4.38}$$

where we have used the property, $u^\beta \nabla_\alpha u_\beta = 0$. We only have a t^r_ϕ component that is only a function of the radius, so the term that goes as $\partial_\phi\left(\sqrt{-g}t^{\phi r}\right)$ is zero. For our choice of metric, $\Gamma^r_{r\phi} = 0$. Furthermore, the indices of $t^{\alpha\beta}$ are symmetric, traceless, and orthogonal to u^α, so we can rewrite

$$t^{\alpha\beta}\nabla_\alpha u_\beta = t^{\alpha\beta}\sigma_{\alpha\beta}. \tag{4.39}$$

We have neglected all z indices, because of our condition to only go to first order in z/r. However, we now wish to height-integrate this equation, and the change of radial gravity with height has an impact. We will expand the Christoffel symbol in equation (4.38) to second order in z/r and apply the height-integration operator

$$\begin{aligned}(\rho_m + p_m)\left(u^r\partial_r u^r + {\Gamma^r_{\alpha\mu}}^{(0)} u^\alpha u^\mu\right) + \\ \frac{1}{2H}{\Gamma^r_{\alpha\mu}}^{(2)} u^\alpha u^\mu \int_{-H}^{H}(\rho+p)z^2 dz + \frac{h^{rr}}{H}\partial_r(p_m H) - u^r t^{\alpha\beta}_m \sigma_{\alpha\beta} = 0.\end{aligned} \tag{4.40}$$

Substituting in equation (4.33)

$$\int_{-H}^{H}(\rho+p)z^2 dz = \int_{-H}^{H} -\frac{g^{zz}\partial_z p}{{\Gamma^z_{\beta\sigma}}^{(1)} u^\beta u^\sigma} z dz = \frac{g^{zz}}{{\Gamma^z_{\beta\sigma}}^{(1)} u^\beta u^\sigma}\int_{-H}^{H} p dz \tag{4.41}$$

where we have integrated by parts and imposed the pressure go to zero outside of $\pm H$. The vertical series expansion of the Christoffel symbols is as in equation (4.28). The radial balance equation is

$$(\rho_m + p_m)\left(u^r\partial_r u^r + {\Gamma^r_{\alpha\mu}}^{(0)} u^\alpha u^\mu\right) + \frac{g^{zz}{\Gamma^r_{\alpha\mu}}^{(2)} u^\alpha u^\mu}{{\Gamma^z_{\beta\sigma}}^{(1)} u^\beta u^\sigma} p_m + \frac{h^{rr}}{H}\partial_r(p_m H) - u^r t^{\alpha\beta}_m \sigma_{\alpha\beta} = 0. \tag{4.42}$$

4.1.6 Angular Momentum

For the angular momentum equation

$$\nabla_\alpha \left(T^{\alpha\beta}\xi_\beta\right) = \nabla_\alpha \left[(\rho+p)u^\alpha u^\beta \xi_\beta + t^{\alpha\beta}\xi_\beta\right] + \nabla_\alpha \left(p g^{\alpha\beta}\xi_\beta\right) = 0 \tag{4.43}$$

$$\partial_r \left[\sqrt{-g}(\rho+p)u^r u_\phi + \sqrt{-g}t^r_\phi\right] = 0. \tag{4.44}$$

This equation is trivial to integrate

$$\sqrt{-g}(\rho+p)u^r u_\phi - C = -\sqrt{-g}t^r_\phi \tag{4.45}$$

$$\rho_0 u^r \left(\frac{\rho+p}{\rho_0}u_\phi - \frac{C}{\sqrt{-g}\rho_0 u^r}\right) = -t^r_\phi \tag{4.46}$$

where C is some constant of integration. From equation (4.19) we know

$$\partial_r(\sqrt{-g}\rho_0 u^r) = 0 \tag{4.47}$$

which allows us to simplify the constant. After height-integrating, our angular momentum equation becomes

$$\rho_{0,m} u^r \left(\frac{\rho_m + p_m}{\rho_{0,m}}u_\phi - j\right) = -t^r_{\phi,m}. \tag{4.48}$$

4.1.7 Energy

The third equation simplification is:

$$u_\beta \nabla_\alpha T^{\alpha\beta} = u_\beta \nabla_\alpha \left[(\rho+p)u^\alpha u^\beta + p g^{\alpha\beta} + t^{\alpha\beta} + T^{\alpha\beta}_{\rm rad}\right] = 0 \tag{4.49}$$

$$-\rho_0 u^\alpha \nabla_\alpha \left(\frac{\rho+p}{\rho_0}\right) + u^\alpha \nabla_\alpha p - t^{\alpha\beta}\nabla_\alpha u_\beta + u_\beta \nabla_\alpha T^{\alpha\beta}_{\rm rad} = 0 \tag{4.50}$$

$$-\rho_0 u^r \left[\partial_r\left(\frac{\rho}{\rho_0}\right) + p\partial_r\left(\frac{1}{\rho_0}\right)\right] - t^{\alpha\beta}\sigma_{\alpha\beta} + u_\beta \nabla_\alpha T^{\alpha\beta}_{\rm rad} = 0 \tag{4.51}$$

where we have used equation (4.5), and $u_\beta \nabla_\alpha u^\beta = 0$. Therefore, our energy equation becomes

$$\rho_0 u^r \left[\partial_r\left(\frac{\varepsilon}{\rho_0}\right) + p\partial_r\left(\frac{1}{\rho_0}\right)\right] = -t^{\alpha\beta}\sigma_{\alpha\beta} + u_\beta \nabla_\alpha T^{\alpha\beta}_{\rm rad}. \tag{4.52}$$

ε is independent of z, as is $p/\rho_0 = c_s^2$. We will replace $p \to p_m$ and $\rho_0 \to \rho_{0,m}$, rather than height-integrating, to agree with the analysis in Chapter 3.

4.1.8 Analytic Newtonian Limit

To prove these equations reduce to the Newtonian case, we assume $\rho_m + p_m \to \rho_m \to \rho_{0,m}$, and that only derivatives in r are significant. Equation (4.48) becomes

$$\rho_m u^r \left(\Omega r^2 - j\right) = -t^r_{\phi,m} = -\alpha r p_m. \tag{4.53}$$

The energy equation simplifies to

$$\rho_m u^r \left(\partial_r \left(\frac{\varepsilon_m}{\rho_{0,m}}\right) + p_m \partial_r \left(\frac{1}{\rho_m}\right)\right) = -\alpha r p_m \partial_r \Omega + u_\beta \nabla_\alpha T^{\alpha\beta}_{\rm rad} \tag{4.54}$$

where we argue that, since radiation should be a local effect, we can make $u_\beta \nabla_\alpha T^{\alpha\beta}_{\rm rad}$ equal to q_{ie} or q^-, as needed. In the Newtonian limit, we take $r_g/r \to 0$ and $(u^r)^2 \to 0$ and $(u^\phi)^2 \to 0$, and equation (4.42) becomes

$$\rho_m \left(u^r \partial_r u^r + \frac{c^2 r_g}{2r^2} - r(u^\phi)^2\right) - \frac{3}{2r} p_m + \frac{1}{H} \partial_r (p_m H) = 0 \tag{4.55}$$

$$\rho_m \left(u^r \partial_r u^r + \frac{c^2 r_g}{2r^2} - r(u^\phi)^2\right) - p_m \partial_r \ln \Omega_K + p_m \partial_r \ln H + \partial_r p_m = 0 \tag{4.56}$$

$$u^r \partial_r u^r + c_s \partial_r c_s = -\frac{c^2 r_g}{2r^2} + r(u^\phi)^2 - \frac{\partial_r p_m}{\rho_m} \tag{4.57}$$

which is equivalent to equation (3.18) with a Newtonian definition of Ω_K. We have now shown each of these equations converges to their non-relativistic counterpart in the proper limit. The set of equations we must solve are

$$\dot{M} = -4\pi \rho_{0,m} H u^r \sqrt{-g} \tag{4.58}$$

$$(\rho_m + p_m)\left(u^r \partial_r u^r + \Gamma^r_{\alpha\mu}{}^{(0)} u^\alpha u^\mu\right) + \frac{g^{zz}\Gamma^r_{\alpha\mu}{}^{(2)} u^\alpha u^\mu}{\Gamma^z_{\beta\sigma}{}^{(1)} u^\beta u^\sigma} p_m + \frac{h^{rr}}{H} \partial_r (p_m H) - u^r t^{\alpha\beta}_m \sigma_{\alpha\beta} = 0 \tag{4.59}$$

$$\rho_{0,m} u^r \left(\frac{\rho_m + p_m}{\rho_{0,m}} u_\phi - j\right) = -\alpha r p_m \tag{4.60}$$

$$\rho_{0,m} u^r \left(\partial_r \left(\frac{\varepsilon_{i,m}}{\rho_{0,m}}\right) + p_{i,m} \partial_r \left(\frac{1}{\rho_{0,m}}\right)\right) = -t^{\alpha\beta}_m \sigma_{\alpha\beta} - q_{ie,m} \tag{4.61}$$

$$\rho_{0,m} u^r \left(\partial_r \left(\frac{\varepsilon_{e,m}}{\rho_{0,m}}\right) + p_{e,m} \partial_r \left(\frac{1}{\rho_{0,m}}\right)\right) = q_{ie,m} - q^-_m. \tag{4.62}$$

4.2 Numerical Implementation

Equations (4.58) through (4.62) define a boundary value problem. Only three of them are differential, and they are all linear and first order. Our choices for quantities to integrate are the dimensionless

$$\vec{y} = \left\{ -\frac{u^r}{c}, \frac{k_B T_i}{\mu_i m_\mu c^2}, \frac{k_B T_e}{\mu_e m_\mu c^2} \right\} \tag{4.63}$$

with derivatives with respect to $x = r/r_g$. We use u^r as an integration variable instead of the Mach number, because it is easier to analytically rewrite the equations. The metric used is typically given in spherical coordinates, so it is converted into cylindrical, and taken to second order in z/r to properly calculate certain Christoffel symbols (see equation (4.28)). Combining the dynamic equations leads to the form

$$\overline{\overline{M}} \cdot \partial_x \vec{y} = \vec{A} \tag{4.64}$$

where the dimensionless $\overline{\overline{M}}$ and $\vec{A}$ contain all of the equation information. At every step, we calculate the matrix numerically, invert, and receive a value for each variable's slope.

We numerically integrate inward from the outer radius using a adaptive fourth-order Runge-Kutta method. Integrating outward from the critical point is numerically unstable, so we must use a shooting method. We must integrate through many orders of magnitude in r and through numerically sensitive regions, so we need a mechanism to change the step size closer to the critical point and the event horizon. At each step, we integrate inward two steps, and, separately, integrate one large step with twice the size. The large step will have more error, but the smaller step will take more computing time. If both methods are not within some percent tolerance of each other, the overall step size is halved and the test is repeated. Once run to completion, this adaptive step algorithm guarantees that we are minimizing computing time by using the largest step size such that the numerical error is below the set threshold. We set the tolerance in the two temperatures and u^r/c_s, rather than the radial velocity, as the Mach number is more sensitive to numerical problems near critical point. The sum of absolute values of percent tolerances for all three variables used was 10^{-10}. Since integration typically requires about 10^5 steps, we should have error on the order of one part in 10^5, so this tolerance is reasonable.

Three boundary conditions for $\vec{y}$ can be set at some radius far away from the black hole where observations can estimate the temperature and density, and therefore the velocity, of the infalling gas. The fourth boundary condition is j, which is found by forcing the solution to pass smoothly through the critical point. We choose to find j by shooting inward using the following algorithm.

Upon integrating to the critical point, the solution curve for u^r/c_s would attempt the behavior of Figure 2.1. For all cases considered, when j is too small, the flow never becomes supersonic, while when j is too large, the flow turns around in r and becomes unphysical. This correlating behavior allows us to use bisection to find the angular momentum eigenvalue. Numerically, if the slope became positive, and was decreasing for the previous 2 steps, the code would assume the solution tried to turn around in radius, and note its location as an upper limit for the critical point. Finding when j was too low is more difficult, as the flow can have many peaks before getting to the one near the critical point. Therefore, the condition for j too low was set if the flow's u^r/c_s came within some small amount (our code used 0.01) of zero. To note the lower limit of the position of the critical point, we chose the peak nearest to the event horizon. It is possible for the code to mislabel which side of the critical point the solution is on if, for example, the solution jumps the critical point, or never gets close to zero.

To find j, we used bisection, with limits of $-2r_g c$ and $2r_g c$, and stopped when the distance between the upper and lower limits of the critical point position differed by a percent of 10^{-10}. The upper and lower limits on j are set to the largest that still maintain solutions that make it to the critical point. Running this algorithm finds an approximate location for the critical point. The last few numerical points curve away from the critical point, so, to approximate a slope with which to jump the critical point, we search the latest solution backward (forward in r) until the slope between successive steps changes by no more than one part in 20, but no more than 100 steps away from the critical point. We then jump the critical point with the slope at this location with twice the distance to the approximate critical point, and continue integrating as before. Manual changing of these numerical parameters was necessary for solutions that failed to integrate properly.

To validate that the code converges with the stated fourth-order, we ran set of convergence tests at the outer radius, and inside the critical point. We integrated inward for a constant step size representative of the initial conditions divided by 1, 2, 4, or 8. Figure 4.1 shows the normalized error in the constituent differential equations, equation (4.59), equation (4.61), and equation (4.62), for the 4 different step sizes. It successfully validates that the code is converging to fourth order.

Figure 4.2 shows the normalized residuals in the five equations, equation (4.59) through equation (4.62), using the adaptive step algorithm for a test that runs through the critical point. The two algebraic equations serve simply to define u^t and u^ϕ, so their errors are determined by machine precision. In the relevant region, the three differential equations mostly remain under a limit even at the critical point. This limit is not the 10^{-10} adaptive step limit we set, because these residuals are not of equation (4.64), but of the constituent equations.

Inputs to the model are the metric, the 3 outer boundary conditions and outer radius, and the following parameters: α and β for the magnetic viscosity and pressure, and $\dot{M}_{\text{out}}$ and s for the mass accretion rate power law. For the validation tests, the non-metric parameters used were the same as for the tests in Section 5.1, but the metric parameters were chosen at random.

4.3 Newtonian Limit

In the Newtonian limit, the equations we have set out to solve should behave like those of Chapter 3 away from the black hole. Using the Schwarzschild metric (see, for example, [18]) and analytically expanding equation (4.58) through equation (4.62) to first order in r/r_g, u^r/c, and ru^ϕ/c yields the equations of Chapter 3.

Figure 4.3a shows the numerical deviation for the boundary conditions and parameters of Figure 3.1 that has the largest discrepancy. The curves agree at large radius, and we expect them to deviate around 10 r_g, since we are essentially adding a few first order terms in r/r_g. However, the mach number visibly deviates around 250 r_g.

To see the source of the difference, let us find an expression for $\partial_r u^r$. In the linear momentum equation, equation (4.59), the only terms that contain a derivative of u^r are

$$(\rho + p)u^r \partial_r u^r \qquad \text{and} \qquad h^{rr}\partial_r p. \tag{4.65}$$

Since the discrepancy happens at relatively large r, we can assume the Newtonian limit and use equation (4.58) to write

$$h^{rr}\partial_r p \sim pv\partial_r \frac{1}{v}. \tag{4.66}$$

The sum of the two terms in equation (4.59) with derivatives is

$$(\rho + p)\left(u^r \partial_r u^r\right) + \frac{h^{rr}}{H}\partial_r(pH) \to \frac{\rho_0}{v}\left(v^2\partial_r v - \frac{p}{\rho_0}\partial_r v\right). \tag{4.67}$$

This decomposition transforms equation (4.59) into

$$\left(\frac{v^2 - c_s^2}{v^2}\right)\frac{\partial v}{\partial r} = f \tag{4.68}$$

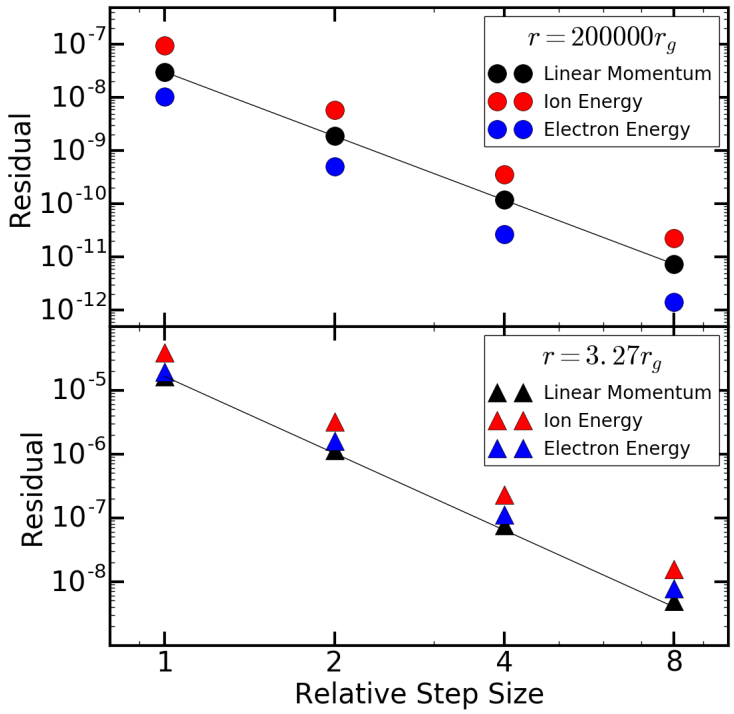

Figure 4.1: Order validation test.
Validation test showing the residual in the constituent equation (not the quantities being integrated) for modulated step sizes. The top graph begins at the outer radius and the bottom plot begins inside the critical point for points on the solution in Figure 4.2. Both are integrated inward for 100 steps at $h = r/200 r_g$ through 800 steps at $h = r/1600 r_g$. The base step size was chosen a factor of 200 lower than the value of the starting location, as the residual for any smaller step size chosen would be dominated by machine precision, rather than numerical integration error. Derivatives in the constituent equations were calculated with a fourth-order implementation. The solid line has the slope for a fourth-order code for comparison purposes.

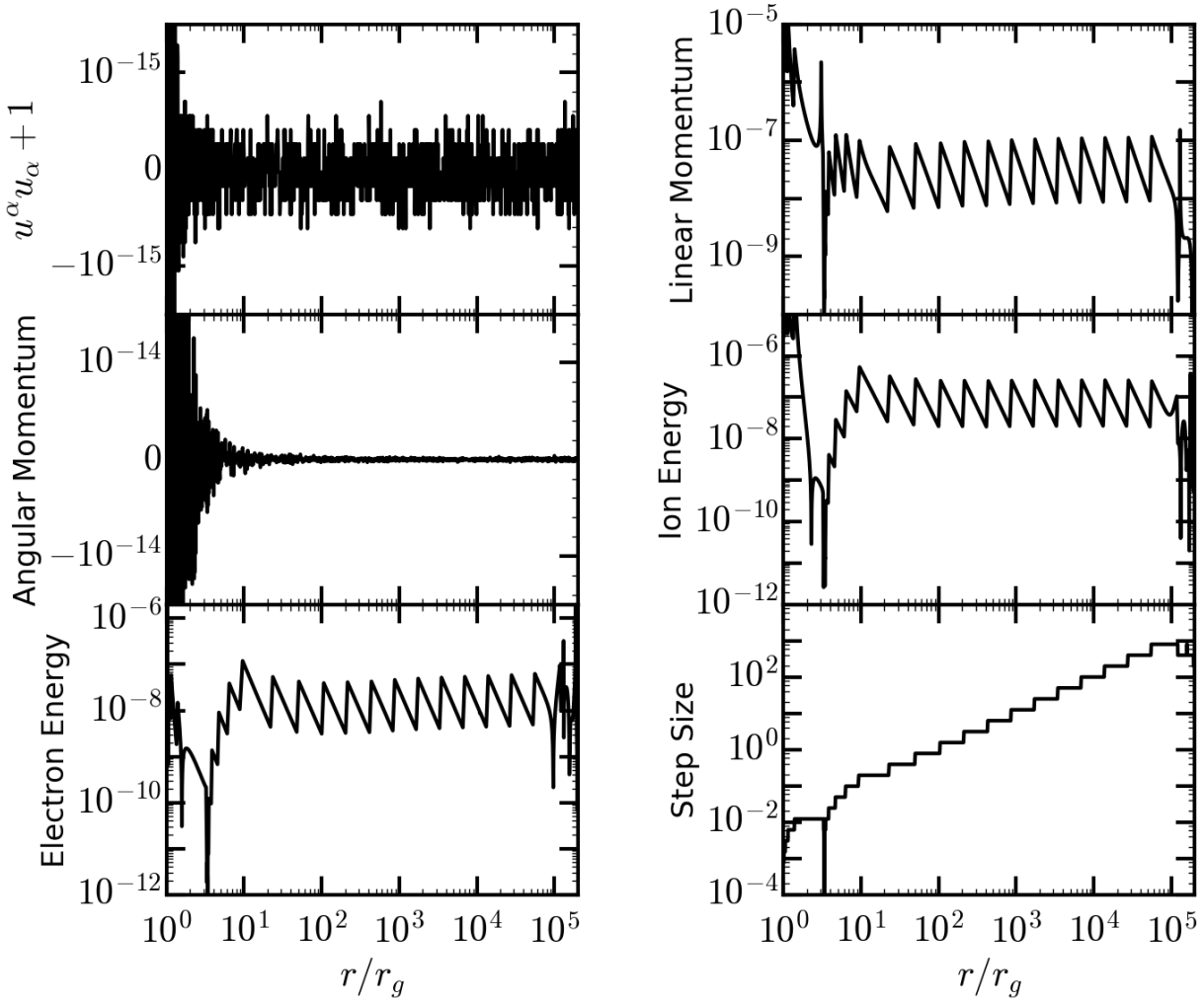

Figure 4.2: Residual test

The first five plots show the residuals in the constituent equations for a adaptive-step solution running through the critical point. As expected, the algebraic equations have an error due to machine precision, and the differential equations have an upper limit on the residuals. The bottom-right plot show the step size adapting, and the critical point at $r = 3.36r_g$. The metric used was as in Section 5.2, for $a = -0.4$, $\alpha_{13} = 0.1$, $\alpha_{22} = 0.2$, $\alpha_{52} = 0.3$, and $\epsilon_3 = 0.4$. Other parameters and boundary conditions are set as in Section 5.1.

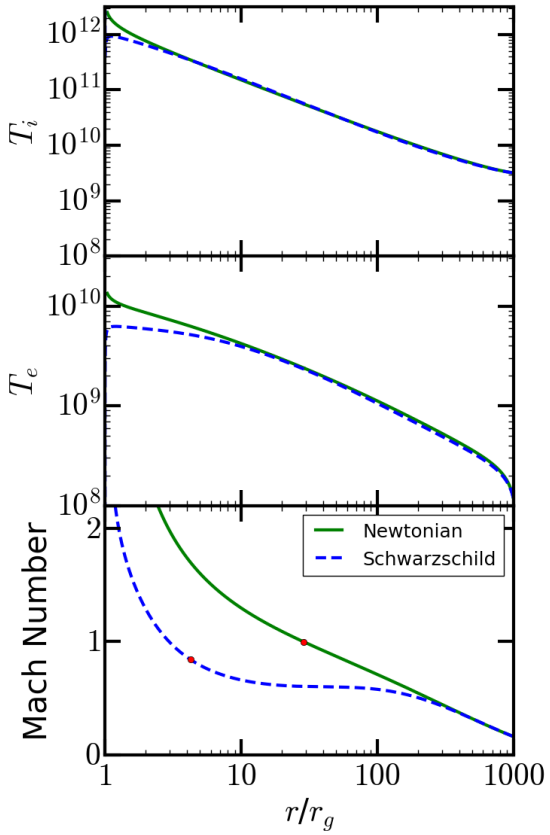

(a) Plot of quantities directly relating to the three integrated variables. The effects of the Schwarzschild metric are of order r/r_g. The ion and electron temperatures visibly deviate around $10r_g$, but the Mach number deviates at $250r_g$. The red point corresponds to the critical point for each solution. Initial conditions and parameters were chosen as in Figure 3.1 for $T_i = 3.2 \times 10^9 K$.

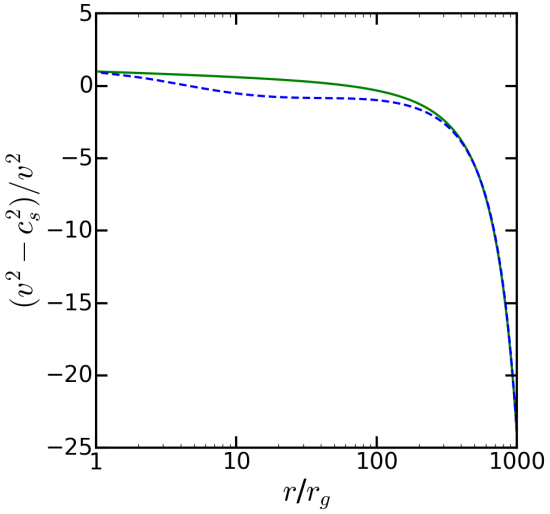

(b) The plotted quantity determines how much the extra terms added into the model due to General Relativity affect the Mach number. Exactly when this quantity falls by an order of magnitude, there is a shift in the dynamics of the accretion flow.

Figure 4.3: Comparison of solutions for a Newtonian and Schwarzschild prescription of gravity.

where f is a function of r, velocity, temperatures, and derivatives of the temperatures. If we take the Newtonian limit of f, we would have the linear momentum equation, equation (3.18). Let us not take the limit, but instead split it into a Newtonian and GR part.

$$\left(\frac{v^2 - c_s^2}{v^2}\right) \frac{\partial v}{\partial r}\Big|_{\text{GR}} = \left(\frac{v^2 - c_s^2}{v^2}\right) \frac{\partial v}{\partial r}\Big|_{\text{Newtonian}} + \epsilon g \tag{4.69}$$

$$\frac{\partial v}{\partial r}\Big|_{\text{GR}} = \frac{\partial v}{\partial r}\Big|_{\text{Newtonian}} + \frac{\epsilon}{\left(v^2 - c_s^2\right)/v^2} g \tag{4.70}$$

where ϵg contains the extra terms added by General Relativity. ϵ depends on r_g/r, $(u^r)^2/c^2$, and $(ru^\phi)^2/c^2$, and is small when the deviation from the Newtonian model occurs. As v approaches c_s, the Newtonian $\partial v/\partial r$ remains constant. This is the critical point smoothness condition. Out at 250 r_g, where the Schwarzschild curve departs, ϵ is around 10^{-2}, but that does not directly indicate a deviation in the mach number of 10^{-2}. Figure 4.3b show a plot of $(v^2 - c_s^2)/v^2$. We can see that the deviation from a Newtonian view occurs when $(v^2 - c_s^2)/c_s^2$ falls by a factor of 10. This means that $\epsilon v^2/\left(v^2 - c_s^2\right)$ is dominating far more than ϵ would suggest. In other words, while we are adding small perturbations, the Mach number is highly sensitive to small changes in gravity.

There is a secondary effect that furthers this discrepancy. In equation (4.59), the gravity and pressure terms dominate by order of magnitude around 250 r_g, so the velocity derivatives correspond to a residual of subtracting far larger quantities. Therefore, large changes in the velocity lead to small changes in the linear momentum equation balance.

We can explain these effects qualitatively. The critical point is located well within the region impacted by General Relativistic effects. The different prescription moves the critical point to a lower radius and lower Mach number. By our assumptions, the flow cannot become supersonic before the critical point. This constrains the Schwarzschild solution to agree with the Newtonian solution only until the flow reaches the value of u^r/c_s of the Schwarzschild critical point.

These effects have significant implications for other metrics, as differences in u^r/c_s show up about 10 times further out than expected from measurements of r_g/r. In turn, the height and angular momentum profiles will be affected.

Chapter 5

Exploring the Impact of Spacetime on Structure

5.1 Kerr

We wish now to explore other spacetimes. In General Relativity, a spinning black hole is described by the Kerr metric [18], and adds a parameter to the model: the spin, a, which corresponds to the angular momentum of the black hole. The Kerr metric has a different ISCO, and introduces many frame dragging effects near the black hole. Terms involving the spin go as $(r_g/r)^2$, so we only expect to see significant deviations around $3r_g$. However, the effects in Section 4.3 extend the deviations to around 60 r_g.

We can get the Mach number initial condition via the number density, but this boundary condition of 100cm^{-3} [2], causes the solution to diverge before reaching the critical point. For that reason, we take the mach number to be the lowest value that could integrate fully inward, or 0.05 at $2 \times 10^5 r_g$, the outer bondi radius. We set $s = 0.27$ and $\dot{M}_{\text{out}} = 10^{-6} M_\odot \text{yr}^{-1}$ in the style of [22]. Note that in Figure 5.1 that the density and temperatures jump around before settling to a solution with outer boundary conditions approximately equal to the observed temperatures and density.

The temperature plots are generally unaffected. The overall effect is to lower or increase the power law power of the mach number near the event horizon. For retrograde spins, we expect gas to have lower angular momentum and, therefore, larger inward velocity. This effect is demonstrated in Figure 5.1.

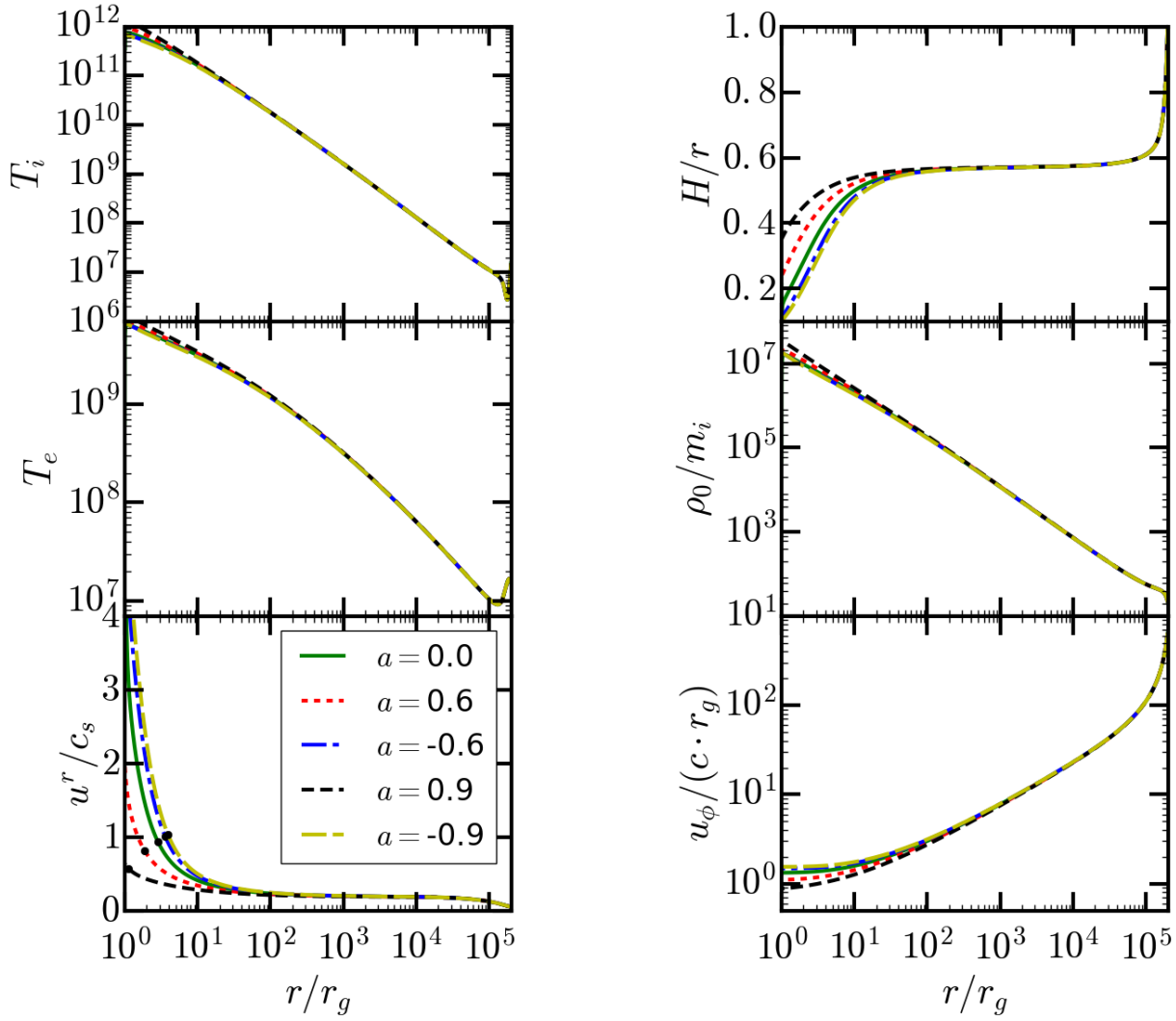

Figure 5.1: Effect of black hole spin on accretion flow solutions.
The effects of black hole spin are only noticeable in the mach number at $r < 60r_g$. The mach number causes changes in the height and angular momentum. There is an decreasing correlation between the spin and mach number. The boundary conditions used are those stated in the introduction and $\alpha = 0.1$ and $\beta = 0.9$. The black dot is the critical point. Note that the event horizon location depends on the spin. All units are in Kelvin or none.

5.2 Parametrized Non-Kerr Metric

To test deviations from General Relativity, we used the metric proposed in [13]. This metric is not a solution to General Relativity, but rather a perturbation to the Kerr metric that preserves the three constants of motion for a test particle: energy, angular momentum, and the Carter constant [7]. As the author of [13] states, the metric is asymptotically flat, has the proper Newtonian limit, and is consistent with parameterized post-Newtonian constraints. In spherical coordinates, the metric is

$$g_{tt} = -\frac{\tilde{\Sigma}\left[\Delta - a^2 A_2(r)^2 \sin^2\theta\right]}{\left[(r^2+a^2)A_1(r) - a^2 A_2(r)\sin^2\theta\right]^2} \tag{5.1}$$

$$g_{t\phi} = -\frac{a\left[(r^2+a^2)A_1(r)A_2(r) - \Delta\right]\tilde{\Sigma}\sin^2\theta}{\left[(r^2+a^2)A_1(r) - a^2 A_2(r)\sin^2\theta\right]^2} \tag{5.2}$$

$$g_{rr} = \frac{\tilde{\Sigma}}{\Delta A_5(r)} \tag{5.3}$$

$$g_{\theta\theta} = \tilde{\Sigma} \tag{5.4}$$

$$g_{\phi\phi} = \frac{\tilde{\Sigma}\sin^2\theta\left[(r^2+a^2)^2 A_1(r)^2 - a^2\Delta\sin^2\theta\right]}{\left[(r^2+a^2)A_1(r) - a^2 A_2(r)\sin^2\theta\right]^2} \tag{5.5}$$

where, to lowest permitted order,

$$\Delta = r^2 - 2Mr + a^2 \tag{5.6}$$

$$\tilde{\Sigma} = r^2 + a^2\cos^2\theta + f(r) \tag{5.7}$$

$$f(r) = \epsilon_3 \frac{M^3}{r} \tag{5.8}$$

$$A_1(r) = 1 + \alpha_{13}\left(\frac{M}{r}\right)^3 \tag{5.9}$$

$$A_2(r) = 1 + \alpha_{22}\left(\frac{M}{r}\right)^2 \tag{5.10}$$

$$A_5(r) = 1 + \alpha_{52}\left(\frac{M}{r}\right)^2. \tag{5.11}$$

We have 4 new parameters, $\alpha 13$, $\alpha 22$, $\alpha 52$, and ϵ_3. If they are all zero, the metric reduces to the Kerr metric. Furthermore, for $a = 0$, α_{22} completely drops out of the metric. For

our purposes, we can define the event horizon as the infinite redshift surface, and as long as $|\epsilon_3| < 1$, it is the same as for the Kerr metric.

Due to the nature of the integration code, the solution for the Kerr metric and this perturbed metric with zero perturbation are exactly the same, so the limiting case test is automatically satisfied. We have essentially added terms of order $(r_g/r)^3$, so we expect these perturbations to only have an effect within 2 r_g even considering the effects of Section 4.3. However, these effects can bring the critical point close to the event horizon, thus greatly varying the flow, and invalidating our inside boundary condition. For that reason, we only consider perturbations that maintain a physical critical point boundary condition. Figure 5.3 through Figure 5.13 show the effects of varying $\alpha 13$, $\alpha 22$, $\alpha 52$, and ϵ_3 for extremal spins. The results are also summarized in Table 5.1. The condition for choosing the metric parameters and spin was numerical stability within an overall range of -0.9 to 0.9. We find that the parameters can have large effects on the location of the critical point, which in turn, changes j. This has an overall effect of offsetting the angular momentum. Therefore, the parameters can cause deviations in the critical point which in turn affects the velocity, height, and angular momentum. In the constituent equations, this corresponds to changes in the radial, azimuthal, and vertical momentum balance equations. Seemingly independently, parameters can cause changes in the temperatures which transfer to the density and pressure. However these effects are limited to near the event horizon and are small in magnitude. Variations in the parameters affect the plots similar to small changes in the spin in Figure 5.1. The deviations could be further attributed to changes in the mass accretion rate or magnetic parameters.

All perturbations increased in magnitude with the spin. At prograde spin, all changes were dominated by the α_{13} and α_{22} parameters. At smaller or more retrograde spins, α_{22} switches its role to only affect the temperatures. The other two parameters, α_{52} and ϵ_3 only have a small effect at highly retrograde spins and only on the temperature quantities.

5.3 Revisiting Assumptions

The shear tensor conditions were only valid for low velocities dominated by rotation. For the test cases considered, these conditions were met outside of $r = 5r_g$ (see Figure 5.2). Any effects nearer to the black hole, especially the critical point boundary condition, are not valid. However, for the domain where these conditions were invalidated, the solutions for the perturbed metric do not strongly deviate from those of the Kerr metric.

Furthermore, we assumed $z \ll r$. This allows there to be missing terms in the constituent equation of order $(H/r)^2$, which, from Figure 5.1, is around 0.25. From height-

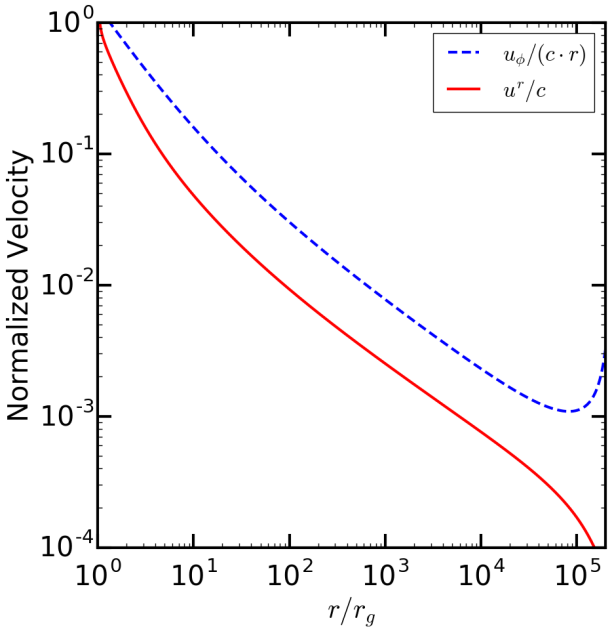

Figure 5.2: Radial and azimuthal velocities for a Kerr black hole accretion flow. Plots of the same quantities in Figure 5.1 so that it highlights the dominating azimuthal components. For the entire flow, the shear requires that u^r is subleading to u_ϕ/r and that both are not close to c.

		α_{13}		α_{22}		α_{52}		ϵ_3	
		0.9	-0.9	0.9	-0.9	0.9	-0.9	0.9	-0.9
$a = 0$	u^r	-0.802	0.564	0.000	0.000	1.371	-1.378	-0.713	0.648
	T_i	-6.198	7.871	0.000	0.000	0.286	-0.289	0.994	-0.999
	T_e	-2.978	3.654	0.000	0.000	0.099	-0.100	0.460	-0.465
	ISCO	3.19	2.79	3.00	3.00	3.00	3.00	2.96	3.04
		0.9	-0.9	0.9	-0.9	0.9	-0.9	0.9	-0.9
$a = -0.9$	u^r	-0.751	0.796	-1.782	2.095	0.622	-0.624	-0.173	0.154
	T_i	-3.454	4.008	-2.832	3.284	0.158	-0.159	0.798	-0.783
	T_e	-1.692	1.931	-1.329	1.520	0.058	-0.058	0.392	-0.386
	ISCO	4.51	4.20	4.49	4.22	4.36	4.36	4.32	4.40
		0.9	-0.8	0.8	-0.9	0.9	-0.9	0.9	-0.9
$a = 0.8$	u^r	4.655	-30.188	-30.132	-2.750	7.253	-7.742	-5.736	5.758
	T_i	-21.501	42.147	54.212	-22.941	0.300	-0.136	-2.025	2.000
	T_e	-10.583	16.340	21.097	-11.273	0.002	0.085	-1.343	1.337
	ISCO	1.80	1.15	1.12	1.84	1.45	1.45	1.45	1.46

Table 5.1: Metric Perturbation Effects on Integrated Quantities
This table shows the percent deviations of u^r, T_i, and T_e at the ISCO for the perturbed metric. Only one metric parameter is being varied in each test. Deviations are mostly limited to a few percent, with the exception of the cases where the critical point condition becomes ill-defined.

integrating the gravity term in the radial momentum equation, we know terms of order z^2/r^2 can have a strong impact on the accretion flow solutions. Nonetheless, we ignored such terms as vertical velocity or derivative terms, so that we agree with prescriptions set forth in earlier literature. Proper height-integration or vertical prescription is an important contributor to the physics of accretion flows and will need future work.

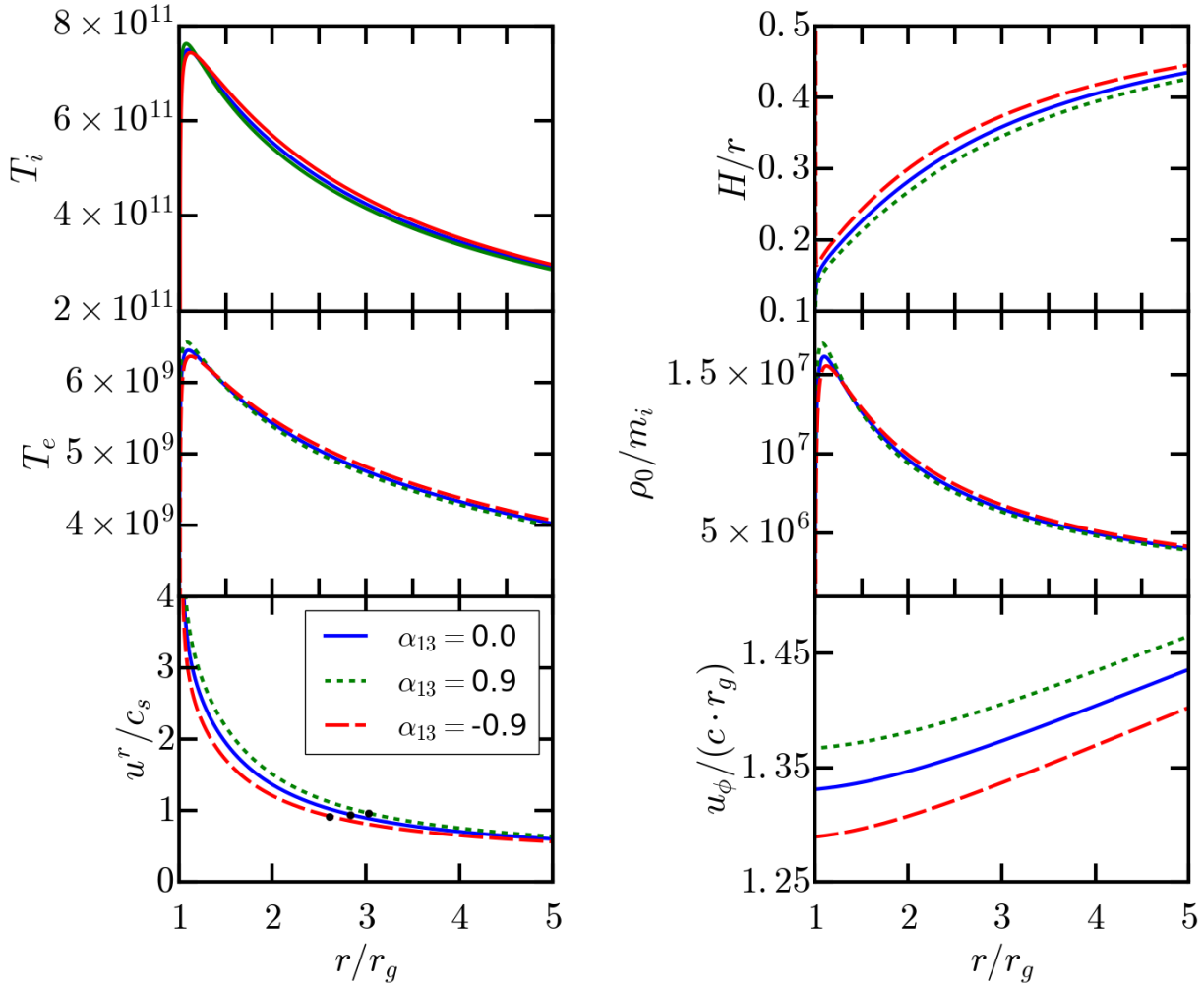

Figure 5.3: Deviations of the accretion flow with a perturbation parameter α_{13} for $a = -0.9$ Plot of structure and dynamics of accretion flow for a perturbed Kerr metric with a black hole spin of -0.9.

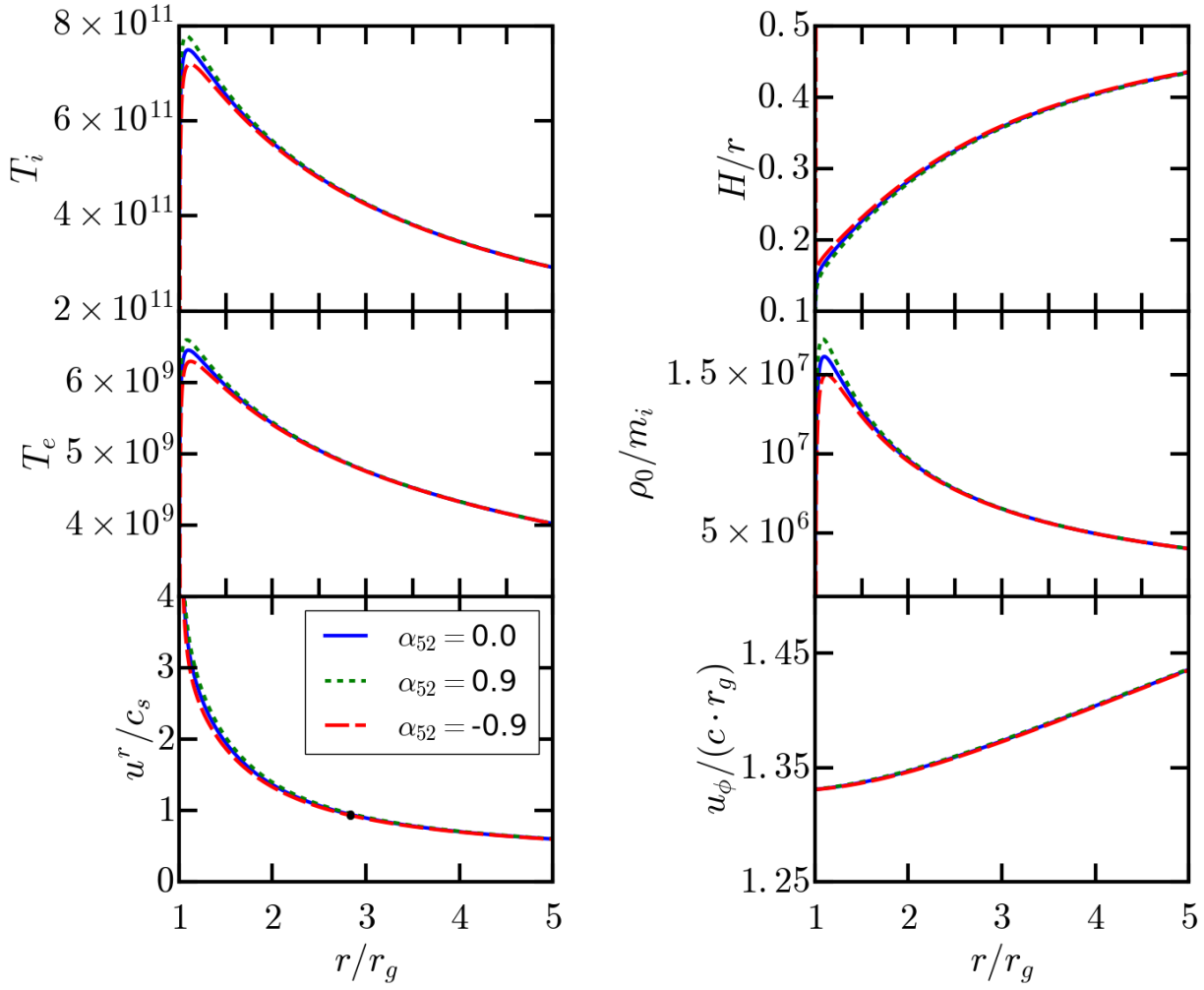

Figure 5.4: Deviations of the accretion flow with a perturbation parameter α_{52} for $a = -0.9$ Plot of structure and dynamics of accretion flow for a perturbed Kerr metric with a black hole spin of -0.9.

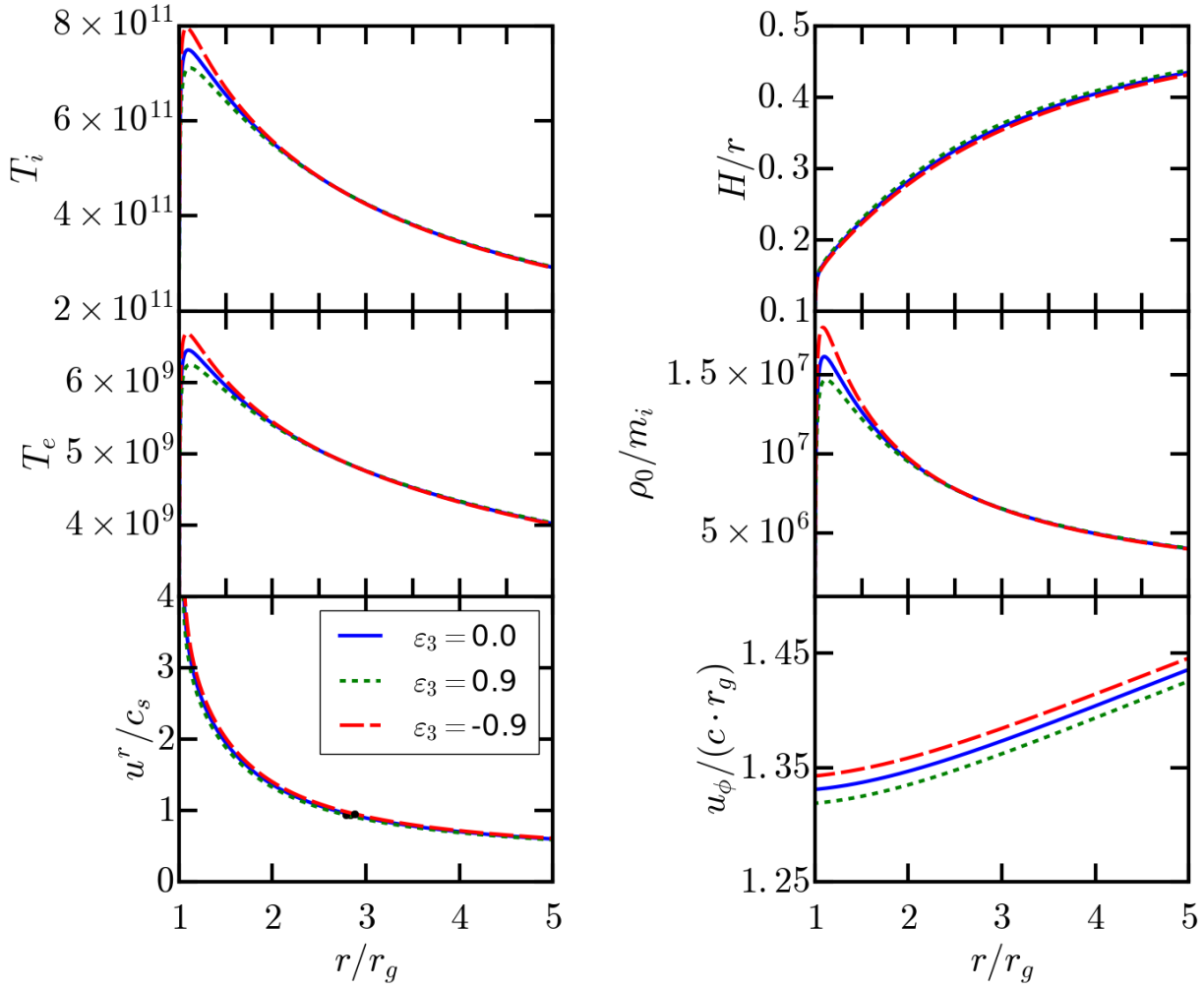

Figure 5.5: Deviations of the accretion flow with a perturbation parameter ϵ_3 for $a = -0.9$ Plot of structure and dynamics of accretion flow for a perturbed Kerr metric with a black hole spin of -0.9.

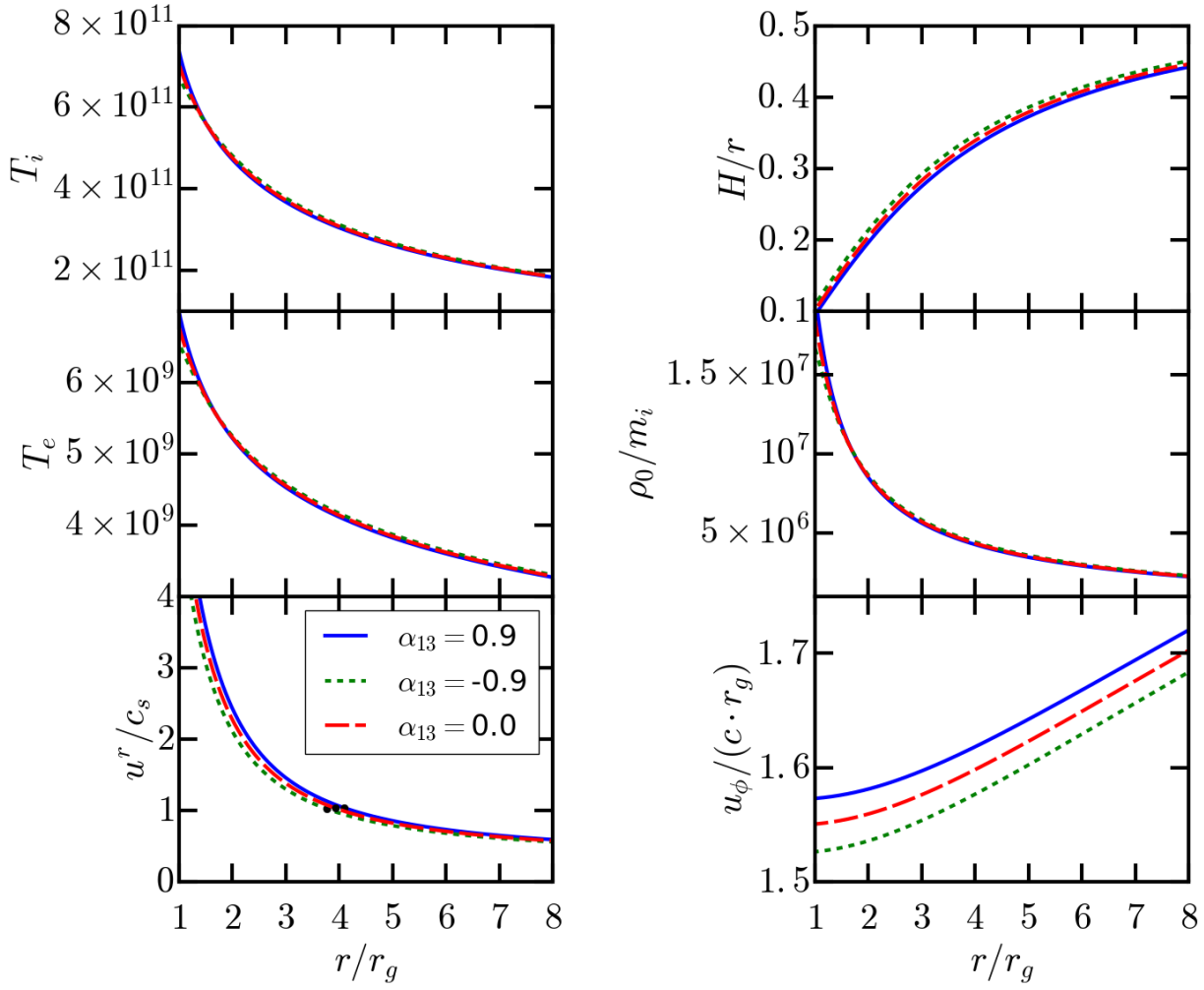

Figure 5.6: Deviations of the accretion flow with a perturbation parameter α_{13} for $a = 0$ Plot of structure and dynamics of accretion flow for a perturbed Kerr metric with a black hole spin of 0.

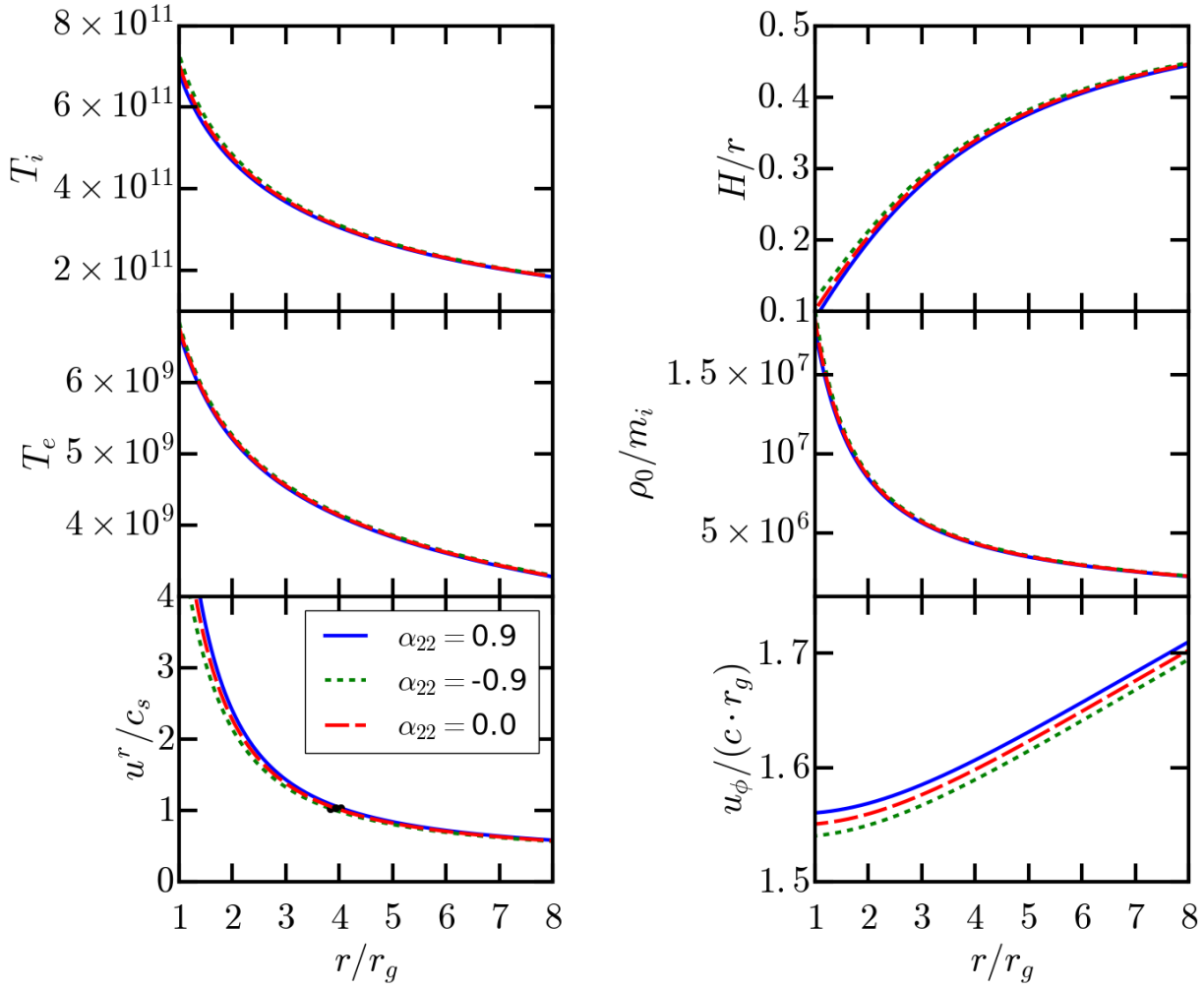

Figure 5.7: Deviations of the accretion flow with a perturbation parameter α_{22} for $a = 0$ Plot of structure and dynamics of accretion flow for a perturbed Kerr metric with a black hole spin of 0.

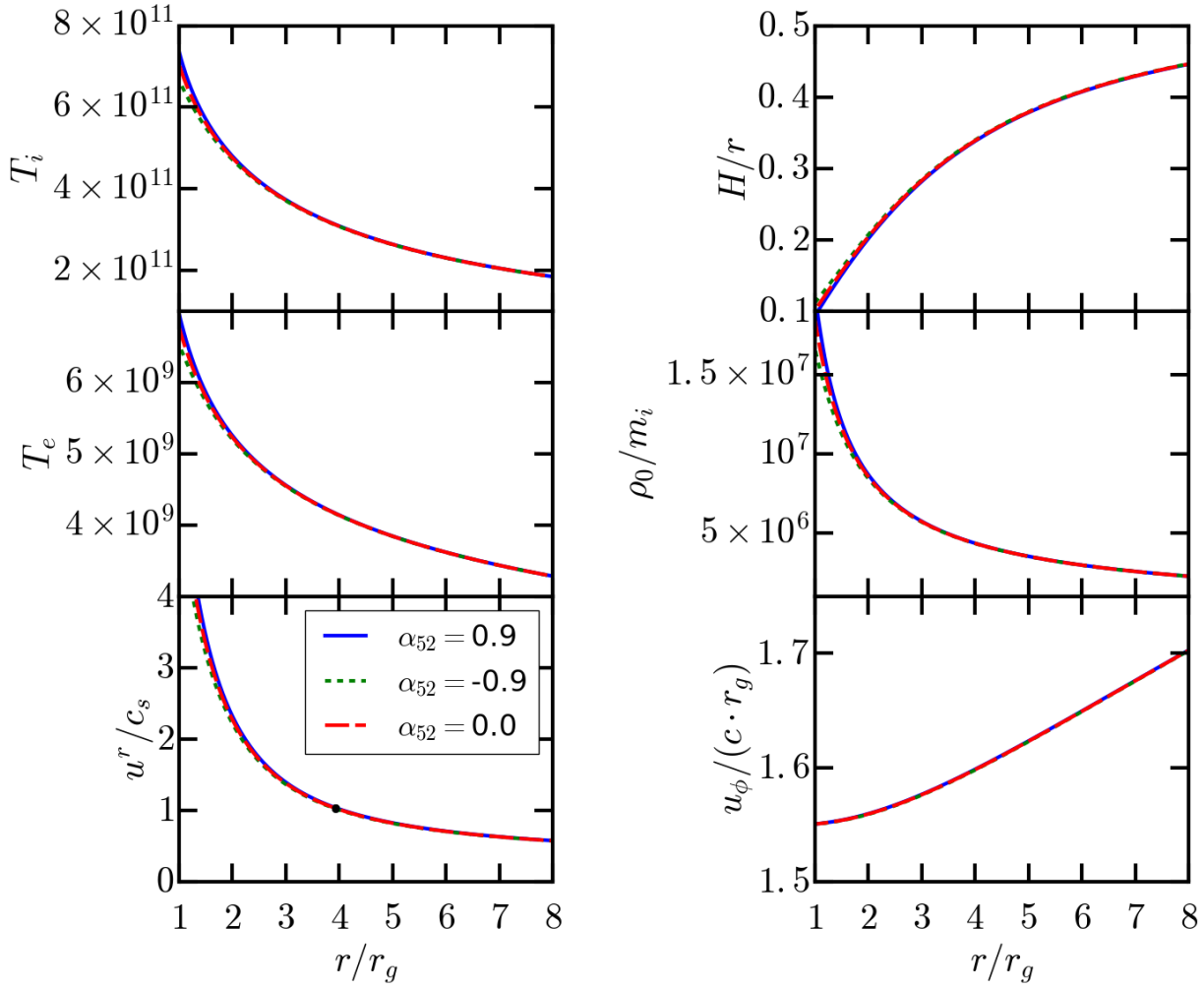

Figure 5.8: Deviations of the accretion flow with a perturbation parameter α_{52} for $a = 0$ Plot of structure and dynamics of accretion flow for a perturbed Kerr metric with a black hole spin of 0.

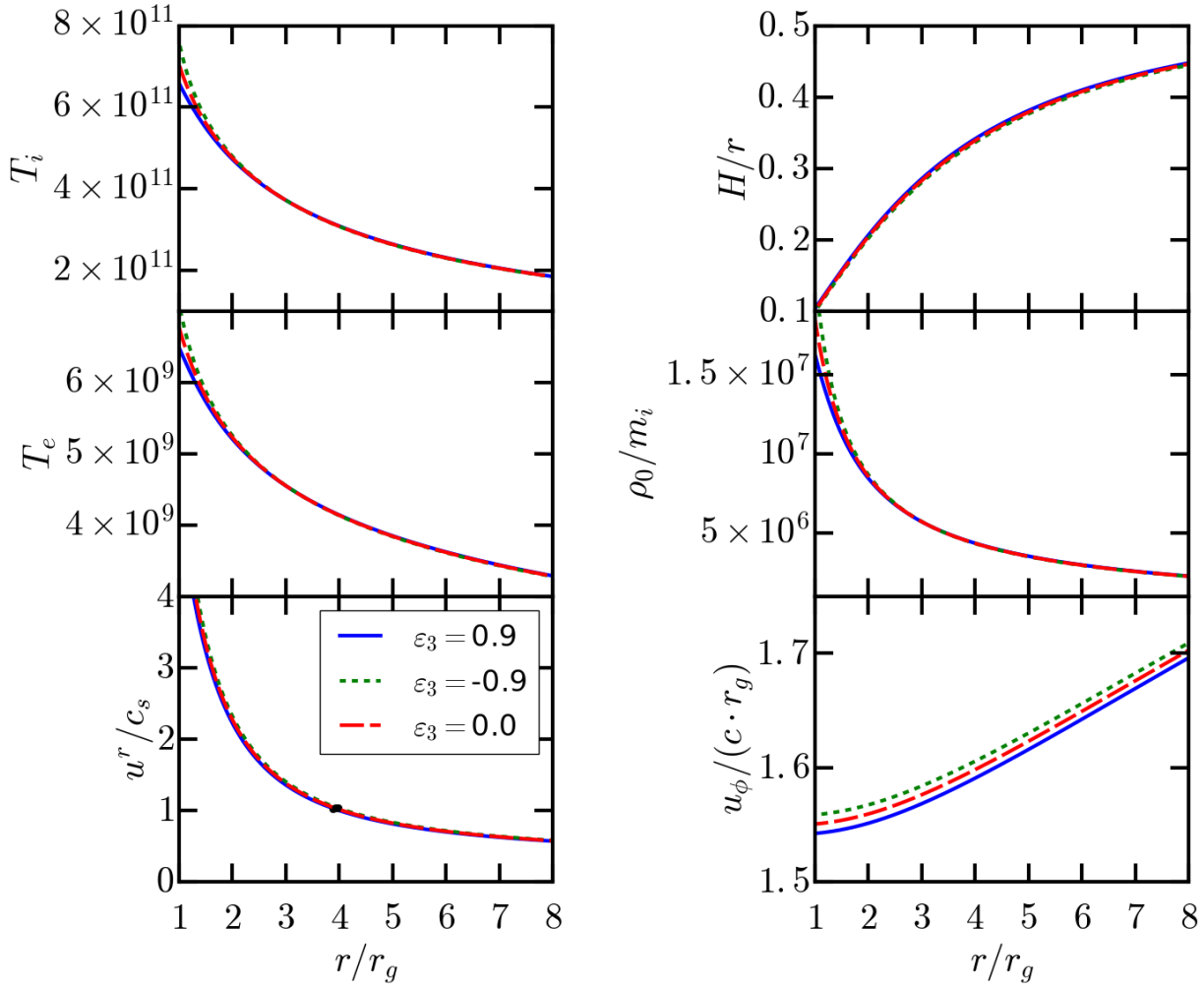

Figure 5.9: Deviations of the accretion flow with a perturbation parameter ϵ_3 for $a = 0$ Plot of structure and dynamics of accretion flow for a perturbed Kerr metric with a black hole spin of 0.

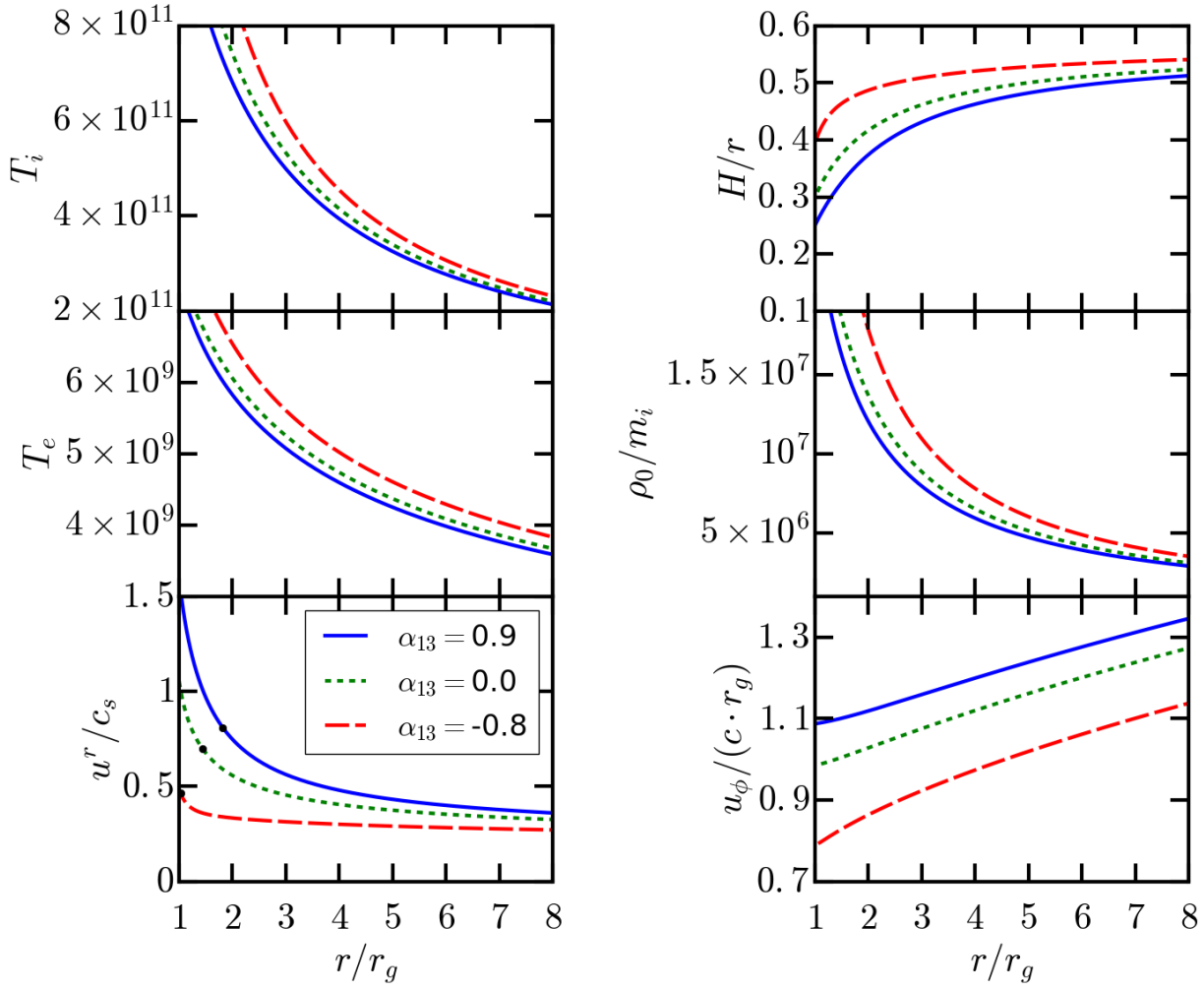

Figure 5.10: Deviations of the accretion flow with a perturbation parameter α_{13} for $a = 0.8$ Plot of structure and dynamics of accretion flow for a perturbed Kerr metric with a black hole spin of 0.8. The lower limit is set to $\alpha_{13} = -0.8$ for stability reasons.

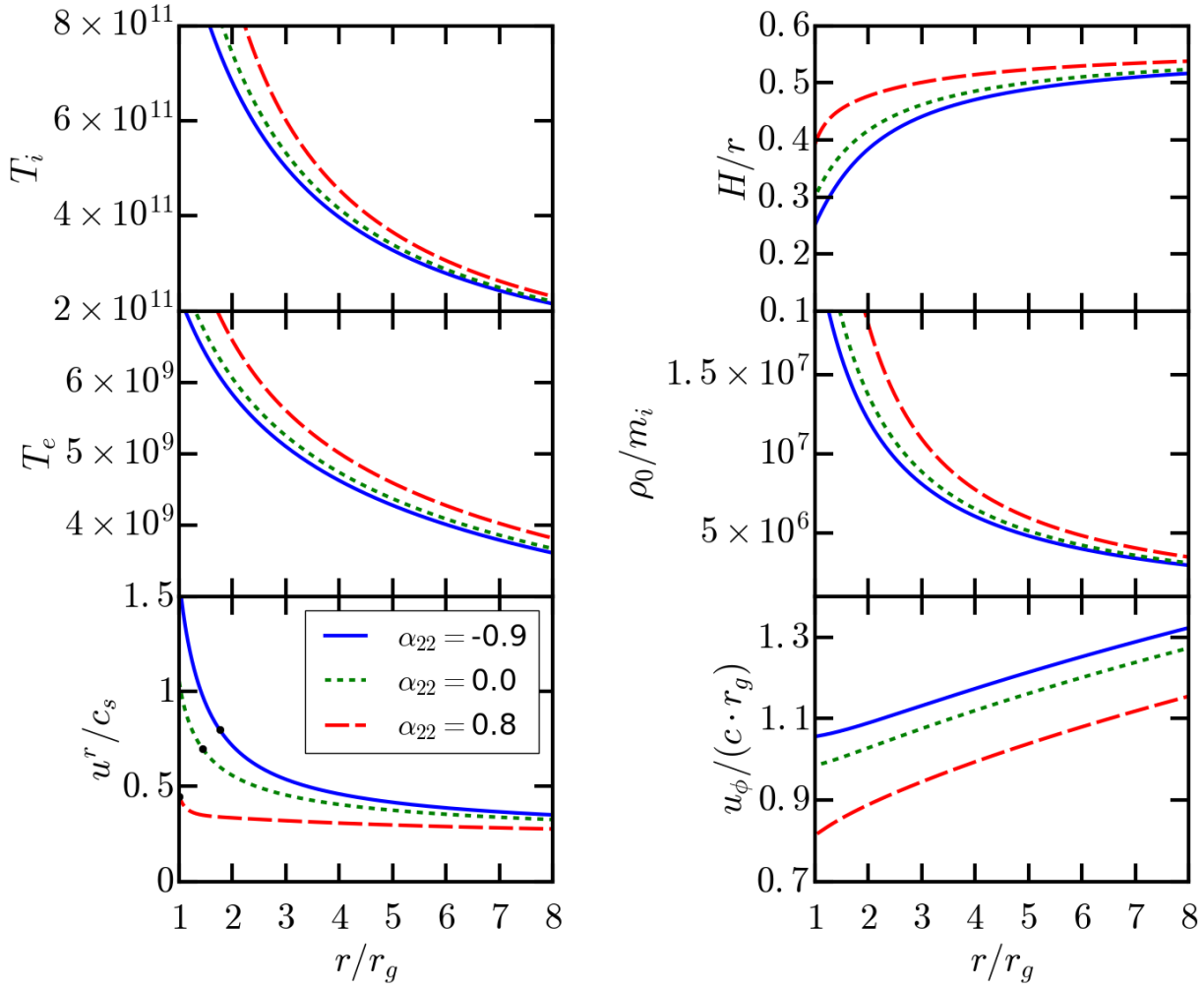

Figure 5.11: Deviations of the accretion flow with a perturbation parameter α_{22} for $a = 0.8$ Plot of structure and dynamics of accretion flow for a perturbed Kerr metric with a black hole spin of 0.8. The upper limit is set to $\alpha_{22} = 0.8$ for stability reasons.

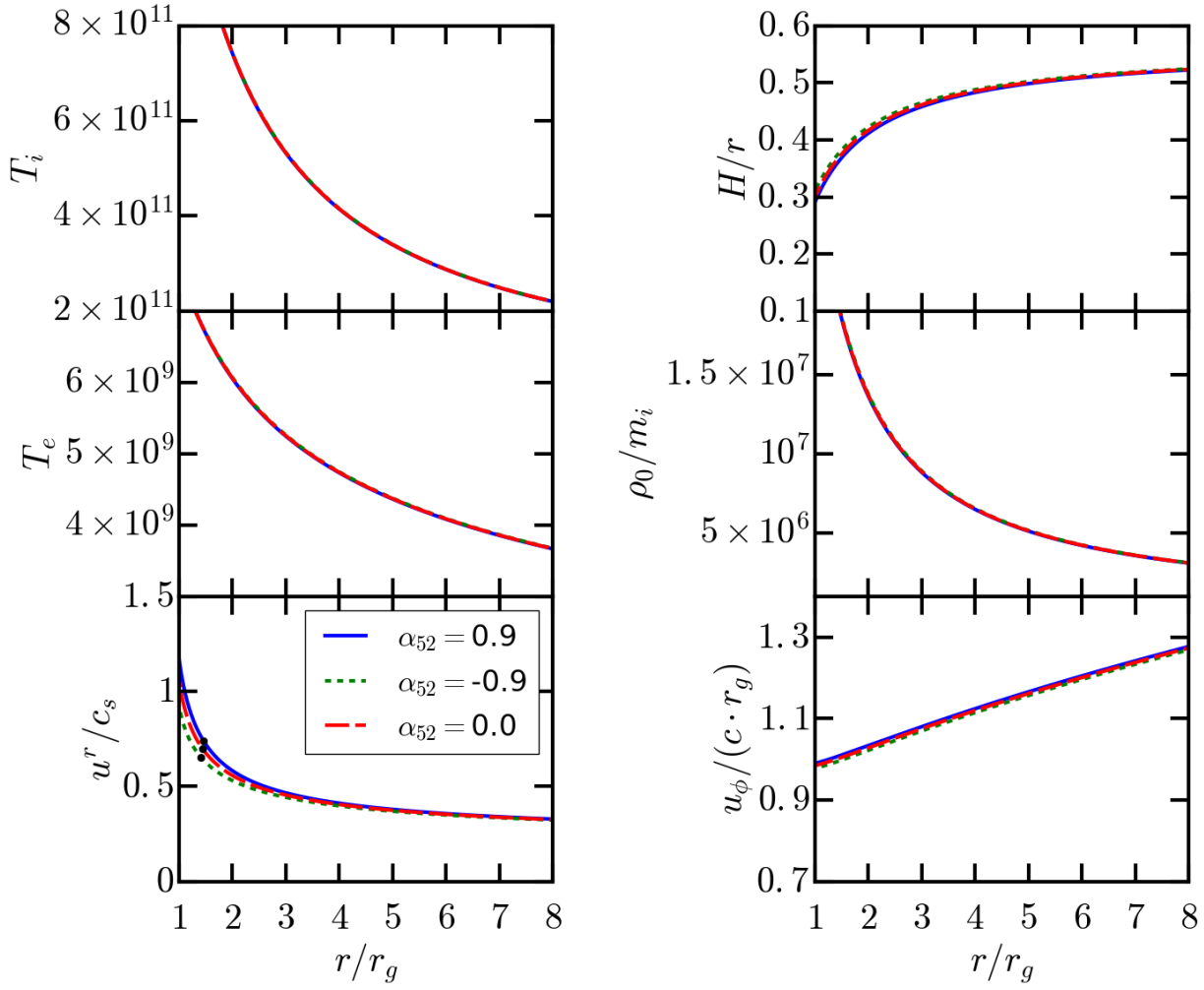

Figure 5.12: Deviations of the accretion flow with a perturbation parameter α_{52} for $a = 0.8$ Plot of structure and dynamics of accretion flow for a perturbed Kerr metric with a black hole spin of 0.8.

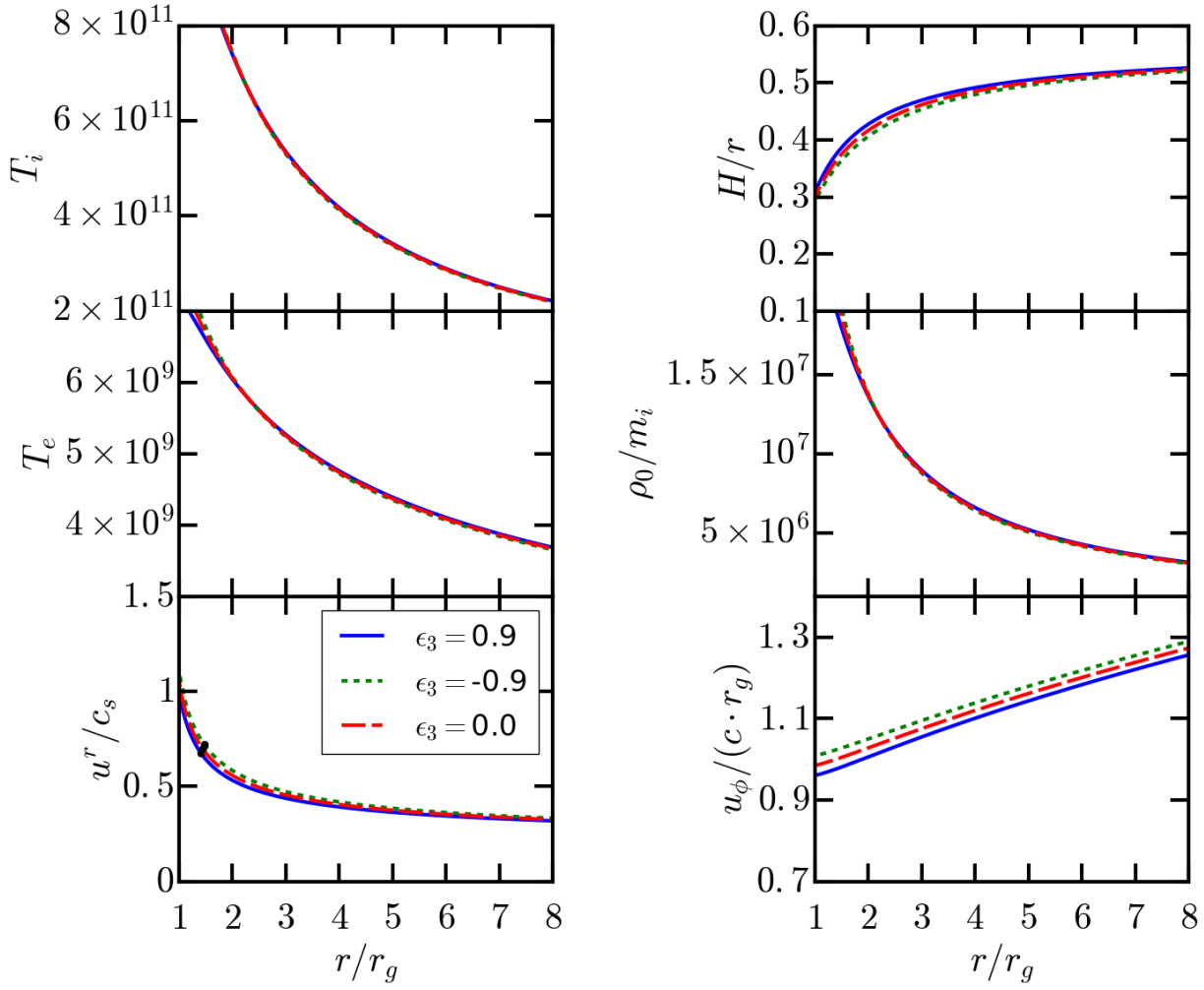

Figure 5.13: Deviations of the accretion flow with a perturbation parameter ϵ_3 for $a = 0.8$ Plot of structure and dynamics of accretion flow for a perturbed Kerr metric with a black hole spin of 0.8.

Chapter 6

Conclusions

The most important product of this project is the creation of a fully covariant semi-analytic accretion flow modeling code capable of using any axisymmetric steady-state metric. It properly takes into account covariant viscosity and vertical momentum to produce profiles of the accretion flow. It can be further applied to explore RIAFs and can be used as an input for EHT imaging code.

We also showed that the impact of general relativity on the velocity, angular momentum, and height of gas in accretion flows can be felt much further away from the black hole than expected. This clearly indicates that including General Relativity in any accretion flow model is not optional.

Furthermore, we performed a series of tests by modifying the underlying spacetime, using a specific quasi-Kerr metric. We find that the changes are limited to a few percent, and appear similar to changes in the black hole spin. These effects can be further masked by different mass accretion rate prescriptions, boundary conditions, and viscosity models. Therefore, the effects of modified metrics on the accretion flow structure would not be easily observable. However, we have removed a systematic uncertainty from the previous studies that did link modified metrics to observable effects through imaging techniques. By limiting possible error, this project helps support claims that the EHT is capable of measuring deviations from General Relativity. The studies in [14] and [5] can now be revisited using proper accretion flow structure and dynamics, and then compared to observational EHT data.

References

[1] M. A. Abramowicz and P. C. Fragile. Foundations of Black Hole Accretion Disk Theory. *Living Reviews in Relativity*, 16:1, January 2013.

[2] F. K. Baganoff, Y. Maeda, M. Morris, M. W. Bautz, W. N. Brandt, W. Cui, J. P. Doty, E. D. Feigelson, G. P. Garmire, S. H. Pravdo, G. R. Ricker, and L. K. Townsley. Chandra X-Ray Spectroscopic Imaging of Sagittarius A* and the Central Parsec of the Galaxy. *The Astrophysical Journal*, 591(2):891, 2003.

[3] S. A. Balbus and J. F. Hawley. A powerful local shear instability in weakly magnetized disks. I - Linear analysis. II - Nonlinear evolution. *The Astrophysical Journal*, 376:214–233, July 1991.

[4] A. Boehle, A. M. Ghez, R. Schdel, L. Meyer, S. Yelda, S. Albers, G. D. Martinez, E. E. Becklin, T. Do, J. R. Lu, K. Matthews, M. R. Morris, B. Sitarski, and G. Witzel. An Improved Distance and Mass Estimate for Sgr A* from a Multistar Orbit Analysis. *The Astrophysical Journal*, 830(1):17, 2016.

[5] Avery E. Broderick, Tim Johannsen, Abraham Loeb, and Dimitrios Psaltis. Testing the No-hair Theorem with Event Horizon Telescope Observations of Sagittarius A*. *The Astrophysical Journal*, 784(1):7, 2014.

[6] Avery E. Broderick, Abraham Loeb, and Ramesh Narayan. The Event Horizon of Sagittarius A*. *The Astrophysical Journal*, 701(2):1357, 2009.

[7] Brandon Carter. Global Structure of the Kerr Family of Gravitational Fields. *Phys. Rev.*, 174:1559–1571, Oct 1968.

[8] S. Chandrasekhar. *An introduction to the study of stellar structure*. 1939.

[9] Jorge Cuadra, Sergei Nayakshin, Volker Springel, and Tiziana Di Matteo. Galactic Centre stellar winds and Sgr A* accretion. *Monthly Notices of the Royal Astronomical Society*, 366(2):358–372, 2006.

[10] Sheperd S. Doeleman, Vincent L. Fish, David E. Schenck, Christopher Beaudoin, Ray Blundell, Geoffrey C. Bower, Avery E. Broderick, Richard Chamberlin, Robert Freund, Per Friberg, Mark A. Gurwell, Paul T. P. Ho, Mareki Honma, Makoto Inoue, Thomas P. Krichbaum, James Lamb, Abraham Loeb, Colin Lonsdale, Daniel P. Marrone, James M. Moran, Tomoaki Oyama, Richard Plambeck, Rurik A. Primiani, Alan E. E. Rogers, Daniel L. Smythe, Jason SooHoo, Peter Strittmatter, Remo P. J. Tilanus, Michael Titus, Jonathan Weintroub, Melvyn Wright, Ken H. Young, and Lucy M. Ziurys. Jet-Launching Structure Resolved Near the Supermassive Black Hole in M87. *Science*, 338(6105):355–358, 2012.

[11] J. Frank, A. King, and D. J. Raine. *Accretion Power in Astrophysics: Third Edition*. January 2002.

[12] A. R. Garlick. The stability of Bondi accretion. *Astronomy and Astrophysics*, 73:171–173, March 1979.

[13] Tim Johannsen. Regular black hole metric with three constants of motion. *Phys. Rev. D*, 88:044002, Aug 2013.

[14] Tim Johannsen, Carlos Wang, Avery E. Broderick, Sheperd S. Doeleman, Vincent L. Fish, Abraham Loeb, and Dimitrios Psaltis. Testing General Relativity with Accretion-Flow Imaging of Sgr A*. *Phys. Rev. Lett.*, 117:091101, Aug 2016.

[15] John Kormendy and Douglas Richstone. Inward BoundThe Search for Supermassive Black Holes in Galactic Nuclei. *Annual Review of Astronomy and Astrophysics*, 33(1):581–624, 1995.

[16] D. LYNDEN-BELL. Galactic Nuclei as Collapsed Old Quasars. *Nature*, 223(5207):690–694, Aug 1969.

[17] Daniel P. Marrone, James M. Moran, Jun-Hui Zhao, and Ramprasad Rao. Interferometric Measurements of Variable 340 GHz Linear Polarization in Sagittarius A*. *The Astrophysical Journal*, 640(1):308, 2006.

[18] C. W. Misner, K. S. Thorne, and J. A. Wheeler. *Gravitation*. 1973.

[19] G. B. Rybicki and A. P. Lightman. *Radiative Processes in Astrophysics*. June 1986.

[20] N. I. Shakura and R. A. Sunyaev. Black holes in binary systems. Observational appearance. *Astronomy and Astrophysics*, 24:337–355, 1973.

[21] Feng Yuan, Qiuhe Peng, Ju fu Lu, and Jianmin Wang. The Role of the Outer Boundary Condition in Accretion Disk Models: Theory and Application. *The Astrophysical Journal*, 537(1):236, 2000.

[22] Feng Yuan, Eliot Quataert, and Ramesh Narayan. Nonthermal Electrons in Radiatively Inefficient Accretion Flow Models of Sagittarius A*. *The Astrophysical Journal*, 598(1):301, 2003.